Nilsson, Jenny A.U.; Döös, Kristofer; Ruti, Paolo M.; Artale, Vincenzo; Coward, Andrew; Brodeau, Laurent. 2013 Observed and Modeled Global Ocean Turbulence Regimes as Deduced from Surface Trajectory Data. *Journal of Physical Oceanography*, 43 (11). 2249-2269. 10.1175/JPO-D-12-0193.1

Observed and Modeled Global Ocean Turbulence Regimes as Deduced from Surface Trajectory Data

JENNY A. U. NILSSON,* KRISTOFER DÖÖS,+ PAOLO M. RUTI,* VINCENZO ARTALE,# ANDREW COWARD,@ AND LAURENT BRODEAU+

* *Climate Modeling and Impacts Lab (UTMEA-CLIM, ENEA), Rome, Italy*
+ *Department of Meteorology/Physical Oceanography (MISU), Stockholm University, Stockholm, Sweden*
# *Technical Unit for Energy and Environmental Modeling (UTMEA, ENEA), Rome, Italy*
@ *National Oceanography Centre (NOCS), Southampton, United Kingdom*

(Manuscript received 1 October 2012, in final form 15 February 2013)

ABSTRACT

A large-scale tool for systematic analyses of the dispersal and turbulent properties of ocean currents and the subsequent separation of dynamical regimes according to the prevailing trajectories taxonomy in a certain area was proposed by Rupolo. In the present study, this methodology has been extended to the analysis of model trajectories obtained by analytical computations of the particle advection equation using the Lagrangian open-source software package Tracing the Water Masses of the North Atlantic and the Mediterranean (TRACMASS), and intercomparisons have been made between the surface velocity fields from three different configurations of the global Nucleus for European Modelling of the Ocean (NEMO) ocean/sea ice general circulation model. Lagrangian time scales of the observed and synthetic trajectory datasets have been calculated by means of inverse Lagrangian stochastic modeling, and the influence of the model field spatial and temporal resolution on the analyses has been investigated. In global-scale ocean modeling, compromises are frequently made in terms of grid resolution and time averaging of the output fields because high-resolution data require considerable amounts of storage space. Here, the implications of such approximations on the modeled velocity fields and, consequently, on the particle dispersion, have been assessed through validation against observed drifter tracks. This study aims, moreover, to shed some light on the relatively unknown turbulent properties of near-surface ocean dynamics and their representation in numerical models globally and in a number of key regions. These results could be of interest for other studies within the field of turbulent eddy diffusion parameterization in ocean models or ocean circulation studies involving long-term coarse-grid model experiments.

1. Introduction

This study aims to follow up and remember the work on Lagrangian diffusion undertaken by Volfango Rupolo, who died prematurely in 2010. It was within this field that he achieved the highest of creativity, and his rather recent 2007 work (Rupolo 2007a) is undoubtedly the fullest and most important example. In that paper, he identified the utility of the relationship between the acceleration and velocity time scales of Lagrangian trajectories, and he separated these trajectories into four homogenous classes according to their correlation and dispersal properties. This classification is better known as trajectories taxonomy and can be used to characterize and separate different turbulence regimes in the global ocean (Rupolo 2007b). He showed that the Lagrangian time scales could be obtained from the inverse use of Lagrangian Stochastic Models (LSMs; e.g., Griffa et al. 1995; Veneziani et al. 2004), proposed a screening method for rationalizing the data analysis using the time-scale relationships, and successfully applied it to both drifter and Argo float observations. In the present study, his data analysis methods have been extended to study and evaluate trajectories from both surface drifters and an ocean general circulation model (OGCM) with different grid resolutions. The drifter data can most accurately be described as quasi-Lagrangian trajectories owing to the fact that, although the buoy is freely drifting in the horizontal plane, it is anchored at

Corresponding author address: Jenny A. U. Nilsson, Climate Modeling and Impacts Lab (UTMEA-ENEA), Via Anguillarese 301, 00123 Rome, Italy.
E-mail: jenny.nilsson@enea.it; j.a.u.nilsson@gmail.com

DOI: 10.1175/JPO-D-12-0193.1

15-m depth by its drogue (e.g., Lumpkin and Pazos 2007), and thus the observed trajectories represent a two-dimensional (2D) approximation of the surrounding flow field.

Taylor (1921) first proposed the idea that the scales of turbulence could be regarded as infinitesimal compared to the scales of the mean flow, thus opening up the possibility for scale separation in dispersal studies. Studies along these lines have been undertaken in numerous works within the field of stochastic ocean modeling—compare references in Griffa (1996), as well as in studies of, for example, tracer cascades in 2D turbulence in fluids (Babiano and Provenzale 2007). Elhmaidi et al. (1993), Pasquero et al. (2001), and Rupolo et al. (1996) discussed and evaluated the possibility of separating the near-surface ocean turbulence in two limiting cases according to the inherent dispersal properties of the flow, that is, the frozen turbulence and fixed-float regimes. Rupolo (2007a) developed this methodology further, proposing the flow separation in four turbulence regimes, classes I–IV, to be applied in the present study. A better understanding of the turbulent motion in the upper-ocean velocities would facilitate an improved parameterization of the subgrid-scale physics in ocean models in terms of the lateral diffusive formulations and the specification of the lateral eddy coefficients. Furthermore, a more accurate numerical representation of the turbulent processes would not only influence the modeled ocean currents but could also have implications on the estimated momentum transports in OGCMs, and, ultimately, be of significance in the framework of global ocean climate modeling (cf. e.g., Jackson et al. 2008).

The main scope of this study is to evaluate the representation of near-surface dynamics in noneddy-permitting (1°), eddy-permitting (¼°), and eddy-resolving (1/12°) OGCM configurations by means of the Rupolo screening technique (Rupolo 2007a), and thereafter compare the outcome with the corresponding results from 20 years of observed drifter tracks. Furthermore, the influence on the dispersal properties owing to the temporal sampling rates of the model output will be addressed and investigated. The impact resulting from an increased grid resolution on the surface circulation will be discussed for crucial regions such as the western boundary current systems and the tropical Atlantic Equatorial Currents and will additionally be put in a global ocean circulation context.

The manuscript is outlined as follows: section 2 provides an overview of the theoretical framework of this study, section 3 describes the drifter observations and the synthetic trajectory datasets, section 4 lays out the design of the numerical experiments, section 5 subsequently presents and discusses the results, and finally section 6 offers some conclusions.

2. Methodology

This section will serve as a summary of the theoretical considerations presented in the study by Rupolo (2007a), and these results will subsequently be applied to trajectory data in a standard Lagrangian framework (cf. LaCasce 2008). The trajectories taxonomy will be specified in order to facilitate the identification of the turbulence regimes in the vicinity of the observed and modeled drifter tracks.

First, the trajectory velocity time series $u(t)$ will be used to calculate the correlation function, the power spectrum, and the absolute dispersion:

$$R(\tau) = \lim_{T \to \infty} \frac{1}{\sigma_U^2 T} \int_0^T u'(t+\tau)u'(t)\,dt, \tag{1}$$

$$P(\nu) = \int_0^\infty R(\tau)\cos(\pi\nu\tau)\,d\tau, \quad \text{and} \tag{2}$$

$$A(t) = \langle |x'(\tau + t) - x'(t)|^2 \rangle, \tag{3}$$

where $u'(t)$ is the perturbed velocity time series, having subtracted the time-averaged velocity along the trajectory [following Davies (1991)] from $u(t)$ over a time interval T. Moreover, σ_U^2 represents the eddy kinetic energy (EKE), τ and ν are time and frequency variables, and $x(t)$ describes the drifter position in time, and the angle brackets indicate an average over the time lag t. The Lagrangian integral time scale T_L can be calculated by integrating Eq. (1) and applying the zero-crossing technique (Mariano and Ryan 2007). The obtained value will indicate the time correlation of the velocity time series, thus providing a measure of the memory of the local ocean dynamics:

$$T_L = \int_0^\infty R(\tau)\,d\tau. \tag{4}$$

Rupolo (2007a) showed that the Lagrangian time scales of velocity T_v and acceleration T_a are related to the Lagrangian time scales, the variances of velocity σ_U^2 and acceleration σ_A^2 using a one-dimensional second-order LSM [cf. appendix A and Sawford (1991)]. Explicit equations for T_v and T_a were derived

$$T_v = \frac{T_L + \sqrt{T_L^2 - 4\dfrac{\sigma_U^2}{\sigma_A^2}}}{2} \quad \text{and} \tag{5}$$

$$T_a = \frac{T_L - \sqrt{T_L^2 - 4\dfrac{\sigma_U^2}{\sigma_A^2}}}{2}, \tag{6}$$

where T_a is finite due to the inherent inertia of the Lagrangian particles. The velocity time scales provide a measure of the memory time scales of the velocity field driven by uncorrelated high-frequency impulses (Griffa 1996), while the acceleration time scales describe how well the stochastic model resolves the acceleration and is related to the correlation of the forcing. Furthermore, from these relations it is clear that both T_v and T_a are complex numbers when $T_L^2 < 4(\sigma_U^2/\sigma_A^2)$. In this case, the corresponding trajectory is typically of a looping nature. The ratio between the oscillatory and the memory time scales is given by the nondimensional parameter

$$\gamma_{\text{osc}} = \frac{\sqrt{4\dfrac{\sigma_U^2}{\sigma_A^2} - T_L^2}}{T_L}. \tag{7}$$

From Eqs. 5 and 6, it is possible, furthermore, to calculate the following acceleration and velocity time-scale ratio for each trajectory:

$$\gamma_R = \frac{T_a}{T_v}, \tag{8}$$

henceforth denoted the ''Rupolo ratio.'' This ratio, as proposed by Rupolo (2007a), along with γ_{osc}, has proven to be a powerful large-scale tool for the separation and categorization of ocean trajectories associated with different dynamical regimes. In his study, the dynamical characteristics of trajectories adhering to different intervals of the Rupolo ratio ($0 \le \gamma_R \le 1$) were described and four dynamical classes were identified, hereafter referred to as ''Rupolo classes.'' The trajectories in each Rupolo class share features in terms of shape, velocity correlation properties, and the relationships between EKE and Lagrangian correlation length scales.

Ocean turbulence covers a wide range of dynamical features, from large-scale low-frequency motions to small-scale high-frequency whirls, and an attempt will be made to accommodate the observed and modeled trajectories in these Rupolo classes (cf. Table 1). The Rupolo ratio can, as an unknown reviewer pointed out, be interpreted as a geometric factor; when it is close to zero and the acceleration is not resolved, the trajectories are characterized by jagged motion, as the particles suddenly change direction, while the γ_R ratio is near one when the acceleration is resolved and the motion is thus much smoother.

TABLE 1. Rupolo-class definitions based on the trajectory taxonomy.

Class	γ_R	γ_{osc}	Typical features
I	<0.2	N/A	Low-frequency motion, high-frequency variability
II	$0.4 < \gamma_R < 0.8$	N/A	Low-frequency motion, no high-frequency variability
III	1	<1	High-frequency motion, meandering
IV	1	>1	High-frequency motion, looper

The Class-I trajectories ($0 \le \gamma_R < 0.2$) are described by large-scale motions influenced by high-frequency variability in the velocity fields. The Class-II data ($0.4 < \gamma_R < 0.8$), on the other hand, show intermediate flow characteristics, such as meandering around low-frequency large-scale structures (i.e., around Class-I data), though they appear to be less influenced by high-frequency motions. The low-frequency motions are typically characterized by geostrophic turbulence (e.g., Hua et al. 1998) and are here described in terms of both Class-III and Class-IV data. The Class-IV trajectories ($\gamma_R = 1$, $\gamma_{\text{osc}} > 1$) are characterized by coherent structures of rapid whirls, typically trapped in eddies with determined length scales, and are often surrounded by Class-III trajectories ($\gamma_R = 1$, $\gamma_{\text{osc}} < 1$) that meander between eddies of different sizes in a less energetic turbulent background field, showing only sporadic looping features.

Given the fact that looping and nonlooping trajectories are often found side by side (cf. Veneziani et al. 2004), an objective separation of trajectories in Rupolo classes is recommended before detailed investigations of the local near-surface ocean dynamics can be undertaken. In what follows, we have adopted the taxonomy-separation method to both observed drifter data and synthetic trajectories obtained from offline integrations of model velocity fields.

3. Model and observational datasets

For the purpose of comparing two-dimensional Lagrangian trajectories from drifter observations with surface-velocity-field output from global OGCMs, an open-source Lagrangian trajectory code [Tracing the Water Masses of the North Atlantic and the Mediterranean (TRACMASS)] was set up for the different OGCM grid resolutions for subsequent integration of synthetic trajectories. A brief technical description of this Lagrangian model and its adaptability is provided in appendix B, and the observational datasets and the different numerical ocean models will be briefly described in the following subsections.

TABLE 2. ORCA grid characteristics, identification of Laplacian L or biharmonic Laplacian B operator for the lateral diffusion of momentum, as well as the parameterization values of the L or B k_{visc}, where L ($m^2 s^{-1}$), B ($m^4 s^{-2}$), and k_{trac} ($m^2 s^{-1}$) coefficients are at the equator.

Configuration	Δy (60°N, 0°) (km)	z levels	L or B	k_{visc}	k_{trac}	Available periods
ORCA1	47, 111	64	L	2×10^4	600	1999
ORCA025 (5 day)	14, 28	64	B	-1.5×10^{11}	300	1991–2001
ORCA025 (6 h)	14, 28	75	B	-1.5×10^{11}	300	1997
ORCA12	3, 9	75	B	-1.25×10^{10}	125	1994–99

a. Drifter observations

Surface drifter data (Niiler and Paduan 1995; Lumpkin and Pazos 2007) were collected and processed by the Atlantic Oceanographic and Meteorological Laboratory (AOML) under the Global Drifter Program, formerly World Ocean Circulation Experiment–Surface Velocity Programme (WOCE-SVP). The observed datasets are kindly made available from 1979 to the present through the Integrated Science Data Management (ISDM) system (http://www.meds-sdmm.dfo-mpo.gc.ca/isdm-gdsi/drib-bder/svp-vcs/index-eng.asp).

These drifting buoys communicate continuously data, via the Argos satellite system, regarding their current positions and other physical/biological parameters depending on the technical equipment of the instrument. All drifters were initially attached to drogues or sea anchors centered at 15-m depths and furthermore equipped with sensors for detecting and reporting the presence or loss of the subsurface drogue. In the case of reported missing drogues, the drifter trajectory was to be disregarded in the data analysis. The position data were postprocessed according to the Hansen and Poulain (1996) protocol, thus the raw drifter-trajectory data were edited for spikes and outliers and hereafter interpolated to uniform 6-h intervals using the optimum interpolation procedure known as "Kriging."

In the present study, observed drifter data were gathered for a 20-yr period (January 1991–December 2010) and ordered in continuous nonoverlapping 64-day segments [in agreement with the chosen time intervals in Rupolo (2007a)]. In total, 46 136 of these were stored for analysis. The drifter positions in these trajectory segments were smoothed by a horizontal boxcar filter in order to reduce signals from inertial and subinertial motions, which is common practice in mesoscale studies (Griffa et al. 1995). It should be mentioned, however, that the data filtering could shift the results toward a higher Rupolo ratio as the trajectories get smoother; however, all datasets have been postprocessed analogously, so this should not have consequences on the data intercomparisons.

b. OGCM configurations

The ocean velocity fields were obtained from fully prognostic configurations of the global Nucleus for European Modelling of the Ocean (NEMO), an ocean–sea ice general circulation model (Madec et al. 2012), and the model experiments were forced using the bulk method along with 6-hourly atmospheric fields of the so-called Drakkar Forcing Set, version 4 (DFS4) from Brodeau et al. (2010). The horizontal resolution of the model configurations varies from coarse (1°; ORCA1, where ORCA stands for Oceanic Remote Chemical Analyzer) to finer eddy-permitting (1/4°; ORCA025) and eddy-resolving (1/12°; ORCA12) grids (cf. Table 2). A detailed description of the ORCA025 configuration and an evaluation of the implemented momentum advection scheme is available in Barnier et al. (2006). The ORCA mesh grid is characterized by a tripolar structure with two north poles located on the Russian and North American continents, respectively, in order to avoid a singular point in the Arctic Sea. The polar areas are better resolved as the size of the grid cells decreases with increasing latitudes; see Table 2 for typical values at 60°N and the equator. The number of vertical levels was either set to 64 or 75 in the model configurations as detailed in Table 2. In the 64-level set up, the gridbox depths ranged from 6 m at surface to ~200 m near the bottom. In the 75-level configurations, there was higher resolution in the upper ocean (~1 m at the surface).

The parameterization of subgrid-scale physics is one of the most uncertain elements in the discretized formulation of the primitive equations (Madec et al. 2012), as small-scale motions have to be described in terms of large-scale features in the ocean circulation. Hence, the choice of advection schemes as well as tracer and momentum diffusion operators to be implemented in the OGCMs is of crucial importance as this determines the transfer balance of kinetic energy and heat at sea surface, and subsequently influences the ocean flow both locally and in a long-term perspective. Here, all the OGCM configurations applied a total variance dissipation (TVD) advection scheme and an iso-neutral Lagrangian tracer diffusion operator, where the horizontal

eddy diffusion coefficient k_{trac} varies with grid size and, thus, also between the different ORCA-grid versions (cf. Table 2 for values near the equator). In ORCA1, the parameterization of the horizontal (lateral) momentum transfer was implemented as a Lagrangian viscosity operator, while the other configurations applied a biharmonic Lagrangian operator. The selected viscosity operators and their corresponding horizontal eddy viscosity coefficients k_{visc} at the equator are provided in Table 2 for all model configurations. The vertical viscosity and diffusion were parameterized as harmonic functions, varying in both space and time, with enhanced vertical diffusion for convection of tracers (all configurations) and momentum (ORCA1 and ORCA025). Furthermore, all configurations applied the same values for the vertical eddy viscosity ($1 \times 10^{-4}\,\text{m}^2\,\text{s}^{-1}$) and the vertical eddy diffusion ($1 \times 10^{-5}\,\text{m}^2\,\text{s}^{-1}$) coefficients.

Lagrangian (second order) operators are typically applied for momentum diffusion in coarse-grid models that do not resolve eddies, in combination with a parameterization of eddy-induced velocity coefficients (Gent and Mcwilliams 1990, hereafter GM90; Killworth 2008), while the biharmonic Lagrangian (fourth order) operator is more suitable for eddy-permitting and eddy-resolving models and do not apply to GM90 eddy-induced velocities. However, as stated by Madec et al. (2012), in all these lateral diffusive formulations, the specification of the lateral eddy coefficients remains a problematic point as there is no really satisfactory formulation of these coefficients as a function of large-scale features.

4. Design of the Lagrangian experiments

a. Time-scale considerations

As numerical model resolution increases, so does the need for large data-storage facilities, and thus compromises are often required in terms of the temporal resolution of the datasets.

Döös et al. (2011) found from their results that the 5-day averaging of the OGCM velocity fields lead to nearly twice as large Lagrangian time scales compared to the results based on model output sampled at a subdiurnal rate. Those results are in agreement with the findings of Garraffo et al. (2001) and McClean et al. (2002) who noted an increase by a factor of ~2 in Lagrangian time scales for synthetic trajectories compared to observations. Garraffo et al. (2001), moreover, suggested that this could be related to the lack of high-frequency wind forcing in the numerical simulations, while McClean et al. (2002) proposed that it could be attributed to the OGCM being too hydrodynamically stable. Garraffo et al. (2001) also state that the observed near-surface Lagrangian velocity time scales could occasionally be underestimated due to the fact that the drifters are not perfect Lagrangian devices and could slip in the water. The presence of spurious acceleration in global surface drifter current data has been investigated by, for example, Grodsky et al. (2011) and Rio (2012), and the influence of slipping undrogued drifters on the resulting global velocity fields is estimated to be around 0.25–0.5 $\text{cm}\,\text{s}^{-1}$.

Rupolo (2007a) stated that in order to obtain reliable T_L estimates, the ratio between the drifter data sampling rate and the Lagrangian time scales should be smaller than 0.2–0.25, or else the calculated time scales would be overestimated. For model fields, this quota is likely to vary with the size of the horizontal grid as the time evolution of the numerical ocean dynamics depends on how (spatially) resolved the ocean processes are, and it would be reasonable to assume that a coarse-grid model would require less-frequent output compared to a high-resolution ocean model. Furthermore, trajectories from high-resolution models with low output frequencies will be smoother compared to those calculated from more-frequent output, because the coarse time-averaging window works as a filter on the data. With these limitations in mind, Lagrangian experiments were undertaken using both 5-day- and 6-h-average ORCA025 output (henceforth denoted ORCA025–5d and ORCA025–6h), and thus a possibility was offered to estimate the influence of the temporal sampling rate on the dispersal properties of the model trajectories. (Global ORCA12 data were unfortunately only available as 5-day-average fields because of the limited storage facilities.)

b. Seeding techniques

The synthetic Lagrangian trajectories were calculated from the modeled Eulerian velocity fields by 64-day-long integrations of the particle advection equation (Döös 1995), starting at the observed initial positions of each observed drifter segment. Due to the fact that there was not access to 20 years of model fields for the three configurations, a seeding strategy that would yield a reasonable global coverage of synthetic trajectories was applied for the initialization of the TRACMASS software. This technique (full seed) implied seeding in all drifter-segment start positions (collected during the period 1991–2010) on their correct days and months, but during one random model year rather than on the actually observed year. This method could be regarded as valid under the assumption that the dispersal properties of the surface trajectories would not vary crucially between one year and another. However, to investigate whether this was the case, an alternative seeding

TABLE 3. Lagrangian time scales as well as velocity and acceleration time scales (days), and Rupolo ratio (i.e., γ_R) along with the corresponding std dev for each dataset and period. Drifter values are based on data from the period 1991–2010 and model values from full-seed experiments during 1997 and 1999 (for those available).

Datasets	Period	T_L	T_v	T_a	γ_R
Drifters	1991–2010	2.7 ± 1.6	2.2 ± 1.7	0.5 ± 0.4	0.24 ± 0.44
	1991–2001*	3.0 ± 1.7	2.4 ± 1.7	0.6 ± 0.5	0.28 ± 0.43
ORCA1–5d	1999	5.0 ± 2.4	4.7 ± 2.4	0.3 ± 1.3	0.06 ± 0.53
ORCA025–5d	1991–2001*	5.6 ± 2.3	4.7 ± 2.2	0.9 ± 1.4	0.20 ± 0.48
	1997	5.7 ± 2.2	4.6 ± 2.1	1.1 ± 1.5	0.24 ± 0.55
	1999	5.8 ± 2.3	4.6 ± 2.1	1.1 ± 1.4	0.25 ± 0.53
ORCA025–6h	1997	3.8 ± 2.1	3.2 ± 2.2	0.6 ± 0.5	0.18 ± 0.39
ORCA12–5d	1997	5.1 ± 2.2	4.1 ± 1.8	1.0 ± 1.8	0.26 ± 0.67
	1999	5.1 ± 2.2	4.0 ± 1.9	1.1 ± 1.7	0.27 ± 0.64

* The results from the ORCA025–5d exact-seed experiment during 1991–2001 are provided along with the corresponding results from the drifter data during this period.

technique (exact seed) was applied where the drifter start positions were seeded on correct dates during a longer-term period (ORCA025–5d; 1991–2001). A comparison between the results from the exact- and full-seed experiments was undertaken in to evaluate if the trajectories based on the model output from one single year could be regarded as representative for the global ocean surface dynamics in a statistical framework.

5. Results and discussion

The results to be presented here aim, in particular, to highlight the scale dependence of synthetic surface trajectories and how their dispersal properties vary with the spatial and temporal resolution of the model velocity fields from which these are computed. The quality of the model surface velocity fields were, moreover, evaluated and to some extent validated by the comparisons made between the observed and synthetic drifter tracks.

a. Seeding sensitivity tests

Sensitivity tests were undertaken to estimate the differences in the model-derived Lagrangian statistics from a long-term period (11 years; exact seed) compared to a random year (1997 and 1999; full seed); the choice of years being dictated by the availability of the model velocity fields (cf. Table 3).

The outcome from the exact- and full-seed techniques using the ORCA025–5d model fields were compared to observations, and the estimated time scales and their corresponding variances (cf. Table 3) were found to be similar, and, moreover, showing nearly twice as large model values as those observed, in agreement with previous results due to Döös et al. (2011), Garraffo et al. (2001), and McClean et al. (2002). Thus, it was concluded that the less costly (in terms of CPU time and storage demand) full-seed method was capable of providing reliable results and could be applied in the forthcoming Lagrangian analyses. Moreover, an interannual sensitivity test was carried out because the model fields at hand would not cover the exact same periods (ORCA1–5d was not available in 1997 and ORCA025–6h was not available in 1999), the results of which are also presented in Table 3. It was established that the resulting time-scale estimates from the different model configurations were roughly equal for these two years, and, therefore, the following trajectory analyses will be based on the integrations of the 1999 model fields, except for the ORCA025–6h configuration, which only yielded data for 1997.

b. "Traditional" Lagrangian analyses

1) ABSOLUTE DISPERSION AND VELOCITY AUTOCORRELATION OF THE TRAJECTORIES

In these numerical experiments, TRACMASS was full-seed initialized and approximately 97% (ORCA1–5d), 98% (ORCA025–5d), 92% (ORCA025–6h), and 98% (ORCA12–5d) of the synthetic trajectories proved to fulfill the 64-day-long model integration criterion during one year (most of the rest stranded). The global-average absolute dispersion after 64 days was 682 km for the drifter observations, compared to 343 (ORCA1–5d), 361 (ORCA025–5d), 393 (ORCA025–6h), and 567 km (ORCA12–5d) for the synthetic trajectories; the dispersion as function of time is provided in Fig. 1. The dashed functions indicate the nearly linear growth of the absolute dispersion in time for $t > T_L$.

The velocity autocorrelation function was calculated for all trajectory datasets, and the results are presented both as total functions (Fig. 2a) and zonal and meridional composites for each dataset (Figs. 2b–f). The Lagrangian time scales were determined by observing the

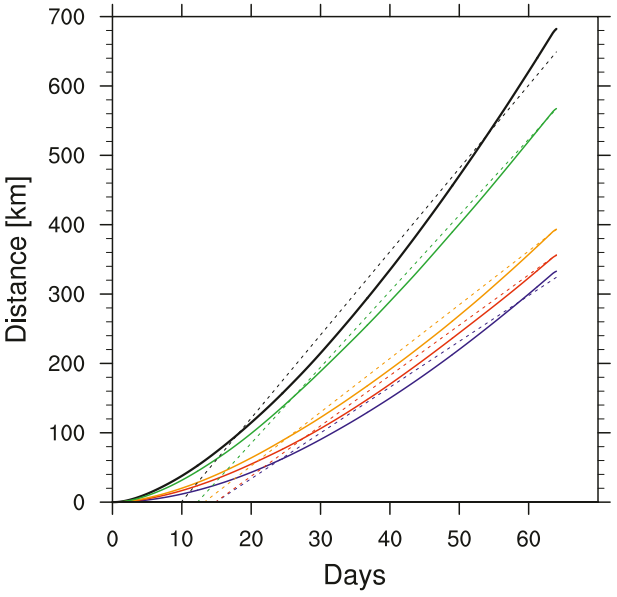

FIG. 1. Global-average absolute dispersion of drifter (black), ORCA1–5d (blue), ORCA025–5d (red), ORCA025–6h (orange), and ORCA12–5d (green) trajectories as a function of time. The corresponding dashed functions indicate the linear growth of the absolute dispersion in time for $t > T_L$.

zero crossings of each function (i.e., integrating until the temporal lag is zero), and the global-average results are presented in Table 3 along with the corresponding standard deviation ranges. A shortcoming with this technique is, however, that it tends to overestimate the integral time scale for trajectories with oscillatory covariance functions—that is, for trajectories trapped in gyres or other coherent structures in the ocean (Mariano and Ryan 2007). The Lagrangian velocity and acceleration time scales were calculated according to the relations in Eqs. (5) and (6) and the Rupolo ratio γ_R [Eq. (8)] was derived from these results and presented in Table 3. These metrics show that the global-average drifter time scales are best described by the results from the high-frequency ORCA025–6h output, while the 5-day-average datasets tend to yield twice as large T_L and T_v values compared to observations. All model configurations except for ORCA1–5d yield reasonable values of the global-average Rupolo ratio. Thus, the relationship proves to cancel out the augmented acceleration and velocity time scales of the 5-day-average fields making the resulting γ_R model values realistic in comparison to that obtained from observations. It is, moreover, noted that the T_L and T_v estimates are fairly well described by the global-average values. However, this is not the case for the T_a and subsequently γ_R as their standard deviations are nearly equal to or, indeed, exceed their average values (typically an indication of the presence of two extreme modes in a distribution).

2) VELOCITY POWER SPECTRA OF THE TRAJECTORIES

Figure 3 presents the global-average total, zonal, and meridional spectral energy distributions of the observed and synthetic trajectory velocity time series. The total power spectra from the drifter observations show the same general characteristics as the corresponding results based on North Atlantic drifters in Rupolo et al. (1996), the numerical results due to Hua et al. (1998), and moreover, the spectra based on Southern Ocean drifters presented by Elipot and Gille (2009). The energy-saturation plateau in the high-frequency band, starting at ~0.6–1 cpd (here separated from the lower frequencies by the dash–dotted line), is related to the dataset grid resolutions. This range is beyond the uncertainty limit of the spectra because the errors in the particle-position tracking increase with the size of the model grid.

It is evident from Fig. 3a that the noneddy-permitting ORCA1–5d configuration fails to reproduce the energy distribution found in the observational dataset. Convergence problems were noted in particular in the low-frequency band, manifested by the oscillating distribution for the zonal velocities (that has contaminated also the total velocity energy spectra). The oscillation is related to the coarse-grid resolution that precludes an accurate simulation of some fundamental parts of the ocean circulation, for example, the western boundary currents and the mesoscale dynamics. The total spectra results from the ORCA025 and ORCA12–5d configurations in Fig. 3a show that these systems manage reasonably well to simulate the general structure of the energy levels over the frequency band. However, both suffer from an energy deficit over all frequencies compared to the observations.

The analysis of zonal and meridional velocity power spectra yields further insights on the anisotropy of the circulation patterns (most likely because of the beta effect and the shape of the global ocean bathymetry), which prove to be of particular importance in the low-frequency range with <0.06 cpd. The meridional data from the higher-resolution models and the observational data asymptote at low frequencies toward a constant value, which implies that the meridional diffusivity is constant, while this is generally not the case for zonal component of the ocean flow.

The intermediate time spectral gradient for the drifter data was found to be rather well described by the scaling law $t^{-5/4}$, consonant with the results due to Elhmaidi et al. (1993) for ensemble dispersion of advected passive tracers in predominately hyperbolical domains (i.e., fixed-float regime behavior). The spectral slope of the ORCA025–6h data (see Fig. 3b) is in best agreement with the observations; this could imply that the relatively

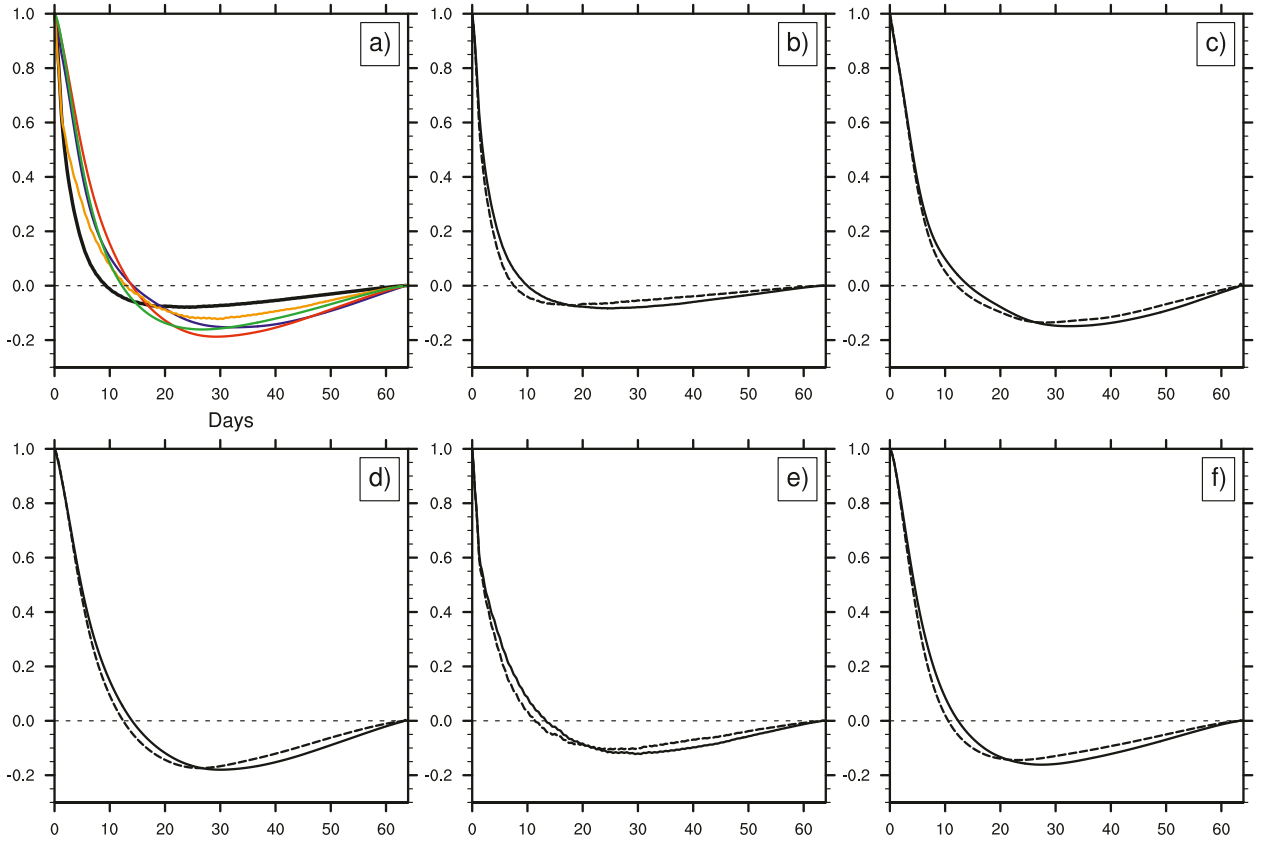

FIG. 2. Velocity autocorrelation functions as a function of time. (a) The total correlation functions are color coded as follows: drifter (black), ORCA1–5d (blue), ORCA025–5d (red), ORCA025–6h (orange), and ORCA12–5d (green). (b)–(f) The zonal (solid) and meridional (dashed) correlation functions are presented for drifter, ORCA1–5d, ORCA025–5d, ORCA025–6h, and ORCA12–5d datasets, respectively.

steeper intermediate-frequency slopes of the 5-day-average data are artifacts owing to the coarse time sampling. If so, this would be an example of the importance of choosing a suitable time-averaging window of the model output fields in order to assure a correct representation of the ocean dynamics. To determine whether this assumption is robust, it is necessary to study more-frequent velocity fields from the ORCA12 configuration. However, presently, because of the large storage demands, this type of analysis has unfortunately not been possible to undertake.

From this first standard Lagrangian analysis, it can be deduced that higher spatial resolution increases the realism of the OGCMs in terms of global-average energy content of the flow for all frequencies and yields the best representation of the global-average absolute dispersion of the synthetic drifters. However, with increasing spatial model resolution, more-frequent model output would be recommended to avoid that the faster smaller-scale motions be filtered by the coarse time-averaged fields. Next, it will be investigated if the synthetic trajectories are capable of describing reasonable turbulence regimes on a global scale compared to drifter observations.

c. *Screening of global trajectory datasets*

The global maps to be presented here, showing the distribution of the Rupolo ratio γ_R and the oscillation index γ_{osc} (Fig. 4 and Fig. 8, described in greater detail below), were created by what is known as binning on a global grid of ¼° × ¼° resolution. Each trajectory point was assigned its corresponding Rupolo-ratio value and averages were computed for all points in the given bins. This technique was tested by Lumpkin et al. (2002) and elaborated by Rupolo (2007a) in order to maximize data coverage within a given study area. A shortcoming of this method could be the spurious influence of nonlocality on the maps due to ''long distance'' trajectories covering different dynamical areas. However, the general impact on the results because of these globetrotting drifters was assumed to be minor and thus disregarded. A Rupolo-ratio map based on 20 years of drifter observations is given in Fig. 4a, and it was noted that these results were in agreement with those presented by Rupolo (2007a) in his Fig. 15a (based on drifter data covering the period 1979–2005, binned on a 1° grid).

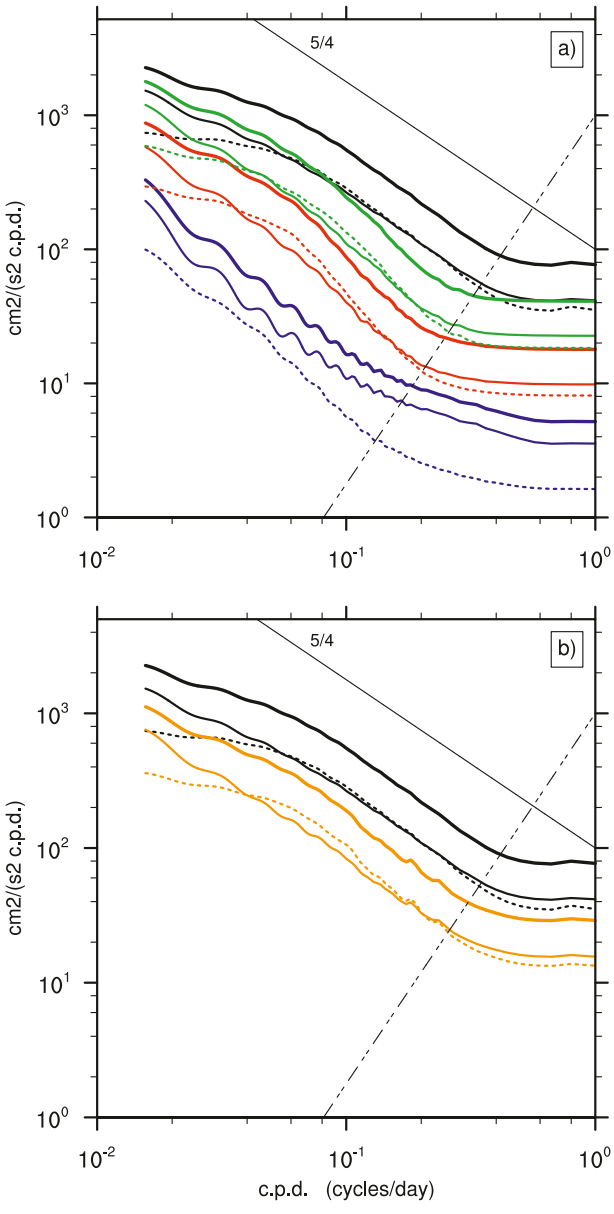

FIG. 3. Power spectra for total (thick solid), zonal (thin solid), and meridional (dashed) trajectory velocities [cm^2 (s^2 cpd)$^{-1}$] as a function of frequency (cpd). The datasets are color coded as follows: (a) drifter (black), ORCA1–5d (blue), ORCA025–5d (red), and ORCA12–5d (green), and (b) drifter (black) and ORCA025–6h (orange). The solid 5/4-slope is associated with ensemble dispersion of advected passive tracers in predominately hyperbolical domains (Elhmaidi et al. 1993), and the dash–dotted line marks the limit of representability of each dataset related to tracking errors of the particle positions.

1) GLOBAL MAPS OF THE RUPOLO RATIO

Global-average Rupolo-ratio estimates based on observed and synthetic trajectory data are provided in Table 3; the observational values being within the limits of those estimated by Rupolo (2007a; their Table 4). The results in Table 3 yield that all the model values are comparable to the observations within the given errors. However, some configurations do better than others. For example, the Rupolo ratio based on the ORCA1–5d trajectories is greatly underestimated compared to the other model configurations, this is due to the fact that the coarse-resolution model cannot resolve the mesoscale dynamics. In Fig. 4b this becomes particularly evident in areas that should be characterized by a high Rupolo ratio, showed γ_R values near 0 instead of $\gamma_R \sim 1$, indicating the obvious fact that the model only sees the mean flow of the meandering current system and its eddies (i.e., the acceleration of the flow is not resolved by the stochastic model).

The γ_R maps based on the ORCA025 datasets presented in Figs. 4c and 4d show similar features compared to the observations in Fig. 4a, with $\gamma_R \sim 1$ (smooth flow) near the western boundary currents and the Antarctic circumpolar current in the Southern Ocean, and $\gamma_R \sim 0$ (jagged currents) in the central parts of the global ocean subbasins. The results from the 6-h-average output yielded distinctly separated smooth regions from adjacent quiescent areas with low γ_R values (even too low compared to observations), while the smooth areas in the 5-day-average velocity fields are more wide stretched, extending into the central parts of the subbasins. Both ORCA025 configurations, and to some extent ORCA12–5d, reveal difficulties in reproducing the smoothness of the North Atlantic inflow to the Arctic Sea, that is, prove unable to resolve the acceleration of the flow in this region. The reason for this could be related to the modeled convection processes in combination with the 2D approximation of the Lagrangian trajectories, or the coupling of the ocean–ice model at high latitudes, or, perhaps, even to the increased horizontal resolution in this area because of the design of the ORCA grid (cf. Table 2).

The maps based on the 5-day-average ORCA12 data proved to be largely characterized by smoother flows than ORCA025, showing high-γ_R values over nearly the entire global ocean. Because the ORCA12 horizontal resolution is to be regarded as eddy permitting, more mesoscale features would be expected to be present in the model output compared to the results from the coarser-grid configurations. However, the ability to create vortices (owing to the finer grid sizes and changed parameterization of the viscosity and tracer diffusion coefficients, cf. Table 2) could also yield increased sources of errors in the surface velocity fields, which should be taken into consideration. But in order complete this error analysis, and to exclude that the inaccuracies in the Rupolo-ratio map are not related to

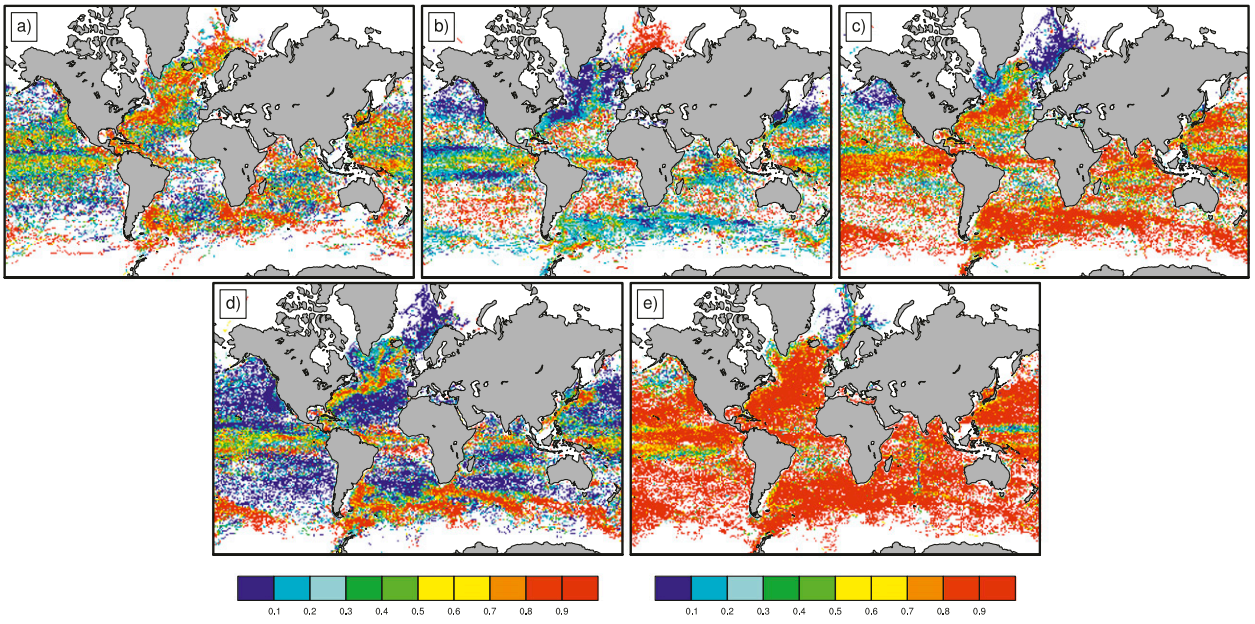

FIG. 4. Rupolo ratio (binned on a 1/4° global grid) derived from (a) drifter observations, as well as synthetic (b) ORCA1–5d, (c) ORCA025–5d, (d) ORCA025–6h, and (e) ORCA12–5d trajectories.

the time averaging of the ORCA12–5d data, a future study dealing with Lagrangian analyses of more-frequent output from this model configuration would be necessary.

The differences of the γ_R fields were qualitatively evaluated through global bias maps in Fig. 5 for the different model configurations (observations–model data) with values ranging from -1 to 1 (0 being a perfect fit). Figure 5a shows that ORCA1–5d fails to simulate the frozen turbulence regimes in western boundary current areas on the Northern Hemisphere, as well as in the Brazil–Malvinas current systems and the Agulhas retroflection zone on the Southern Hemisphere. The bias maps based on the ORCA025–5d and ORCA025–6h data in Figs. 5b and 5c show some improvements in the boundary current areas except for the northernmost parts of the Atlantic Ocean (to be compared with Figs. 4c and 4d), however, the ORCA025–6h velocity fields are too jagged in the interior of the basins compared to observations. Figure 5d show that the ORCA12–5d fields achieve the best γ_R estimates (bias $\rightarrow$ 0) in the boundary-current areas, but provide overall too-smooth trajectories in the global ocean, as evident also from Fig. 4e.

In summary, the spectral energy content in the ORCA12 dataset was found to be the closest to the observed values (cf. Fig. 3), compared to the ORCA1–5d and ORCA025–5d data within the observed frequency range. However, detailed studies showed that the global-average ''eddy energy'' in the ORCA12–5d system was not always located in the correct regions, but rather was homogeneously distributed over the entire modeled global ocean, thus yielding an exaggerated amount of smoothly looping data in the interior of the global ocean subbasins. The relatively realistic energy distribution of the global-average ORCA12–5d spectra could, in part, be due to the fine tuning of the model configuration, while the excess smoothness in areas that should be characterized by highly variable quiescent flow could be the product of an insufficient application of spatially varying eddy-diffusivity coefficients in the diffusion operators.

2) GLOBAL-AVERAGE DISTRIBUTIONS OF THE RUPOLO CLASSES

Global-average distributions of the observed and modeled Rupolo classes were calculated and the results are illustrated by the histograms in Fig. 6. The relative percentages for each class and dataset are provided in Table 4 as well as the average γ_R (for Class I and II) and γ_{osc} (for Class III and IV) values with standard deviations; to be compared with the values obtained by Rupolo (2007b; their Table 7). The standard deviation of the global-average γ_R values in Table 3 indicated the presence of two extreme modes in the data distribution, and this is clearly visible in Fig. 7 for both the observed and modeled datasets.

The presence of looping trajectories in the drifter data in Fig. 6a is around ~30%, in general agreement with the estimates due to Veneziani et al. (2004) who reported 15%–40% of loopers among floats in the western North Atlantic. The Rupolo-class distributions of the

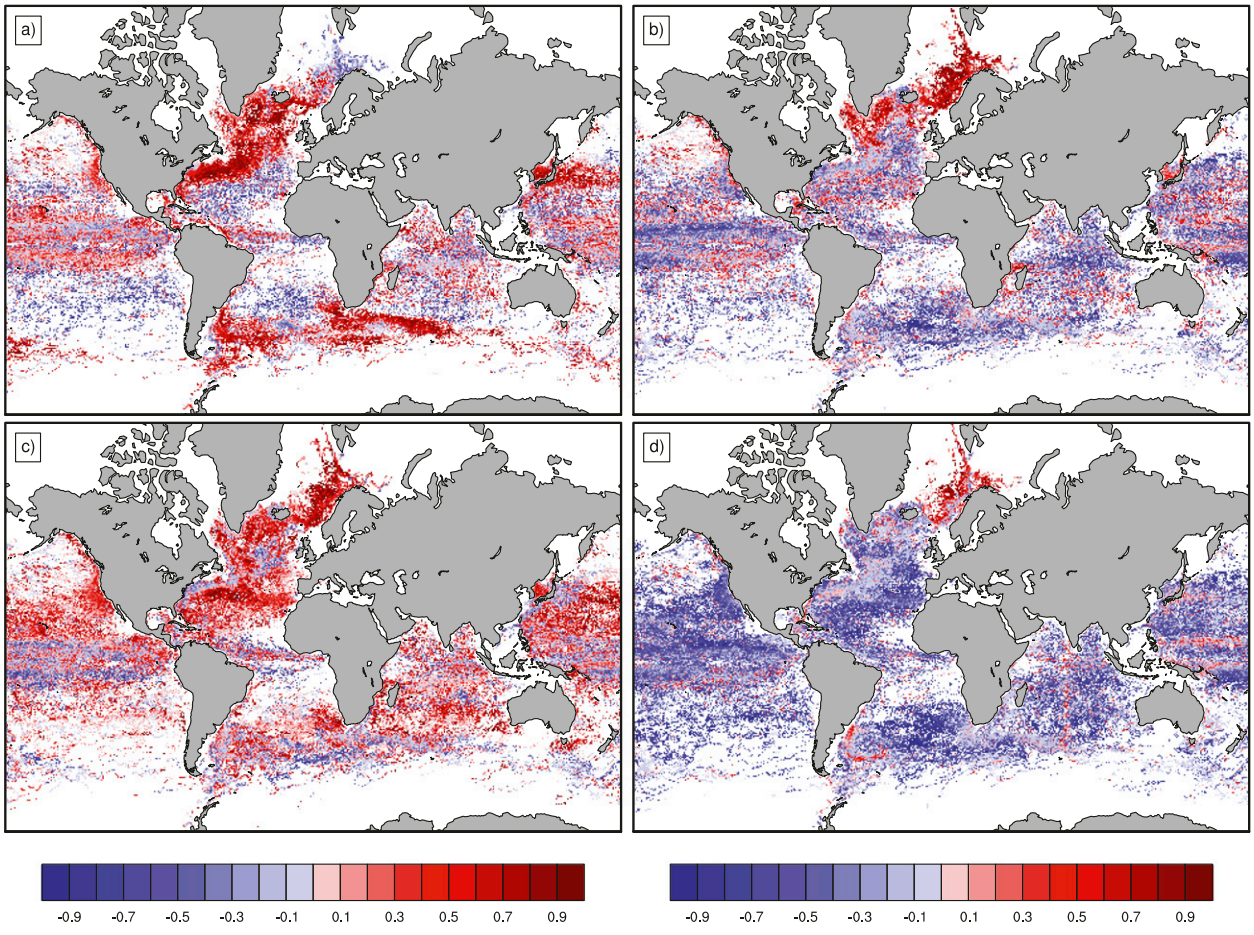

FIG. 5. Global Rupolo-ratio bias. (a) Observations:ORCA1–5d fields, (b) observations:ORCA025–5d fields, (c) observations:ORCA025–6h fields, and (d) observations:ORCA12–5d fields.

drifter and ORCA1–5d data were found to be in surprisingly good agreement (although the amount of modeled Class-I trajectories is slightly underestimated), however, clearly for the wrong reasons (cf. Table 3 and Figs. 4a,b). Both the ORCA025–5d and ORCA12–5d distributions in Figs. 6c and 6e show a large increase of looping trajectories (~45% and ~75%, respectively) and too-little Class-I trajectories ($\gamma_R < 0.2$) compared to the drifter data, as also indicated by the results in Fig. 4 and Table 4. The ORCA025–6h distribution showed, on the other hand, less looping trajectory data (~20%) and an increased amount of Class-I data (~65%) probably owing to the 6-h sampling of the model output that allows more high-temporal variability in the surface velocity fields, thus yielding more Class-I trajectories. This should also be the reason why the Rupolo-class distributions based on 5-day-average fields from the other model configurations yield less data in the range $\gamma_R < 0.2$ compared to observations.

In conclusion, the eddy-permitting and eddy-resolving models accurately simulate the Lagrangian time scales of the western boundary currents (cf. Fig. 5). However, as the horizontal resolution increase, spurious smoothness tends to dominate the 5-day-average global velocity fields. The large amount of Class-III and Class-IV trajectory data in the ORCA025–5d and ORCA12–5d datasets in areas that should be characterized by low γ_R (cf. Fig. 4) is likely due to the poor time sampling of the model fields that yields too-smooth trajectories.

3) OSCILLATION AND MEMORY TIME-SCALE DISTRIBUTIONS

A complication with the Rupolo-class distributions presented in Fig. 6 is that it is not possible to discern the relative distributions of Class-III and Class-IV data because these are both described by $\gamma_R = 1$. To distinguish the presence of meandering trajectories and trapped loopers in the datasets, another type of histogram was created based on the γ_{osc} distributions (cf. Fig. 7).

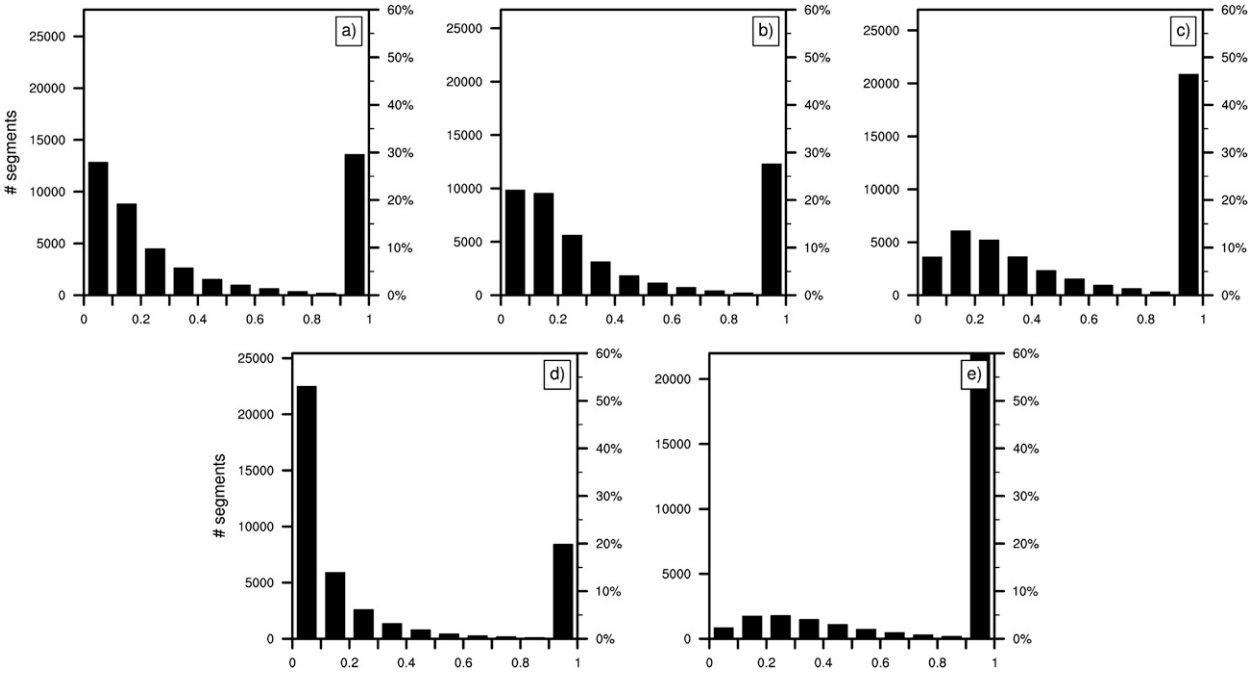

FIG. 6. Global-average Rupolo-ratio distributions from (a) drifter observations, as well as (b) ORCA1–5d, (c) ORCA025–5d, (d) ORCA025–6h, and (e) ORCA12–5d simulations. Please note the varying scales of the left ordinate axis in the plots because of the slightly different total number of segments in each distribution, and that the 60% limit of the right ordinate axis truncates the ORCA12 data at $\gamma_R = 1$ (exact value 76.6%) for higher visibility of the distributions.

The drifter data in Fig. 7a show the presence of both sporadically looping Class-III (freely meandering in the turbulent background field) and Class-IV trajectories (trapped in eddies), with local maxima on each side of the limit $\gamma_{\text{osc}} = 1$ (cf. Table 4). This type of bimodal distribution was not reproduced in either of the 5-day-average outputs; however, the 6-hourly ORCA025 data in Fig. 7d proved able to roughly capture this feature. The distributions of the ORCA1–5d and ORCA025–5d data (cf. Figs. 7b,c) were found to be skewed toward the meandering Class-III regime, while the ORCA12–5d data lean toward the trapped-looper Class-IV regime, and it appears as if the upgrade from eddy-permitting (1/4°) to eddy-resolving (1/12°) grids has led to an overall regime shift of the looping nature of the surface currents.

The global distribution of Class-III and Class-IV trajectories is given in Fig. 8, where it is found from observations that the grand part of the ocean currents are in meandering mode, while trajectories trapped in eddies are mostly present in areas characterized by highly active mesoscale dynamics, such as the Gulf Stream detachment area and in other western boundary current systems, along the equator and in the Arctic region. From the model results, the best representation of the γ_{osc} fields appears to be provided by the ORCA025–5d configuration (cf. Fig. 8c).

d. *Regional trajectory studies*

Separating observed and modeled trajectories in Rupolo classes as part of the Lagrangian analyses yields

TABLE 4. Relative percentages of Rupolo classes for each dataset, along with corresponding average values and std dev of γ_R (Class I and II) and γ_{osc} (Class III and IV).

Datasets	Class I (γ_R)	Class II (γ_R)	Class III (γ_{osc})	Class IV (γ_{osc})	Residuals
Drifters	47.1%, 0.09 ± 0.05	7.6%, 0.54 ± 0.10	22.4%, 0.59 ± 0.24	7.1%, 1.15 ± 0.10	15.8%
ORCA1–5d	43.4%, 0.10 ± 0.05	9.1%, 0.54 ± 0.10	24.6%, 0.56 ± 0.23	2.8%, 1.13 ± 0.11	20.1%
ORCA025–5d	21.5%, 0.12 ± 0.05	11.9%, 0.54 ± 0.10	36.7%, 0.58 ± 0.24	9.5%, 1.18 ± 0.13	20.4%
ORCA025–6h	66.9%, 0.06 ± 0.05	3.8%, 0.53 ± 0.10	10.4%, 0.59 ± 0.25	9.3%, 1.22 ± 0.10	9.6%
ORCA12–5d	7.0%, 0.12 ± 0.05	7.0%, 0.54 ± 0.11	41.8%, 0.66 ± 0.23	34.8%, 1.23 ± 0.14	9.4%

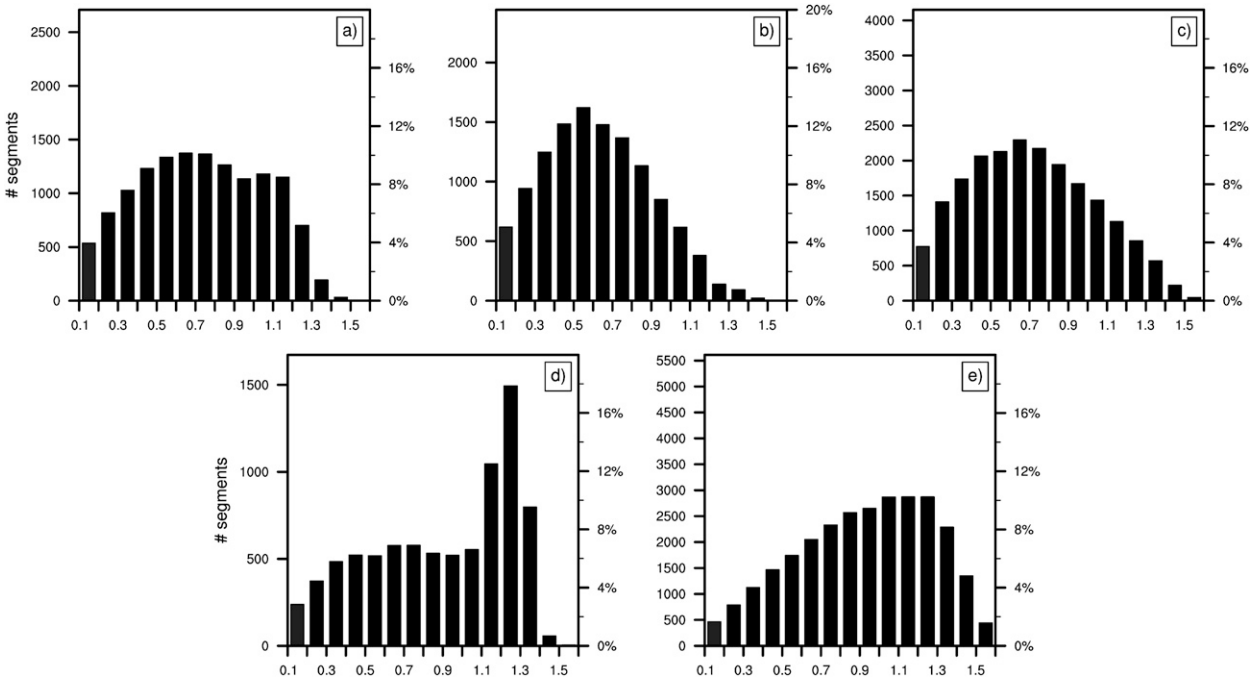

FIG. 7. Histogram of the dimensionless parameter γ_{osc}, which describes the relation between the oscillatory and the memory time scales of the trajectories globally. (a) Drifter observations, as well as (b) ORCA1–5d, (c) ORCA025–5d, (d) ORCA025–6h, and (e) ORCA12–5d simulations. Please note the varying scales of the ordinate axis in the subplots.

information of the flow characteristics that could not have been obtained by traditional methods (e.g., EKE or looper and no-looper analyses). Figure 9 illustrates observed drifters crossing westward the 20°E meridional in the Agulhas retroflection area, and the trajectories have been grouped according to their corresponding Rupolo classes. This figure provides an example of the typical characteristics of these dynamical

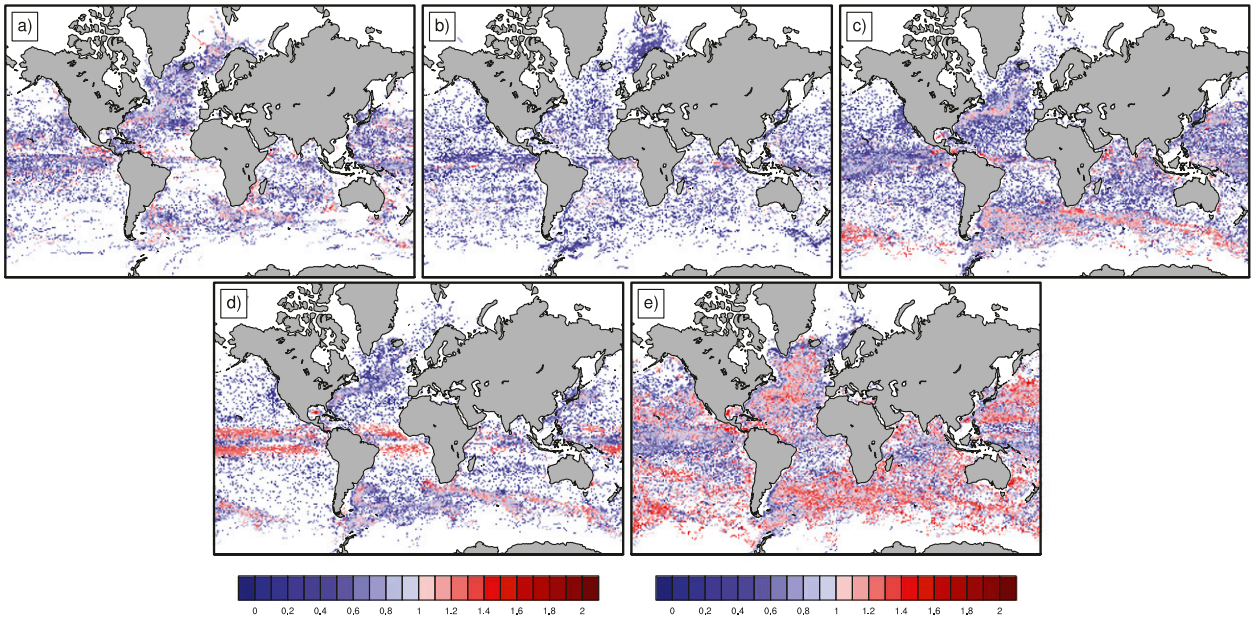

FIG. 8. Rupolo Class-III ($\gamma_{osc} < 1$) and Class-IV ($\gamma_{osc} > 1$) distributions, binned on a $^1/_4°$ global grid, for (a) drifter observations, as well as synthetic (b) ORCA1–5d, (c) ORCA025–5d, (d) ORCA025–6h, and (e) ORCA12–5d trajectories.

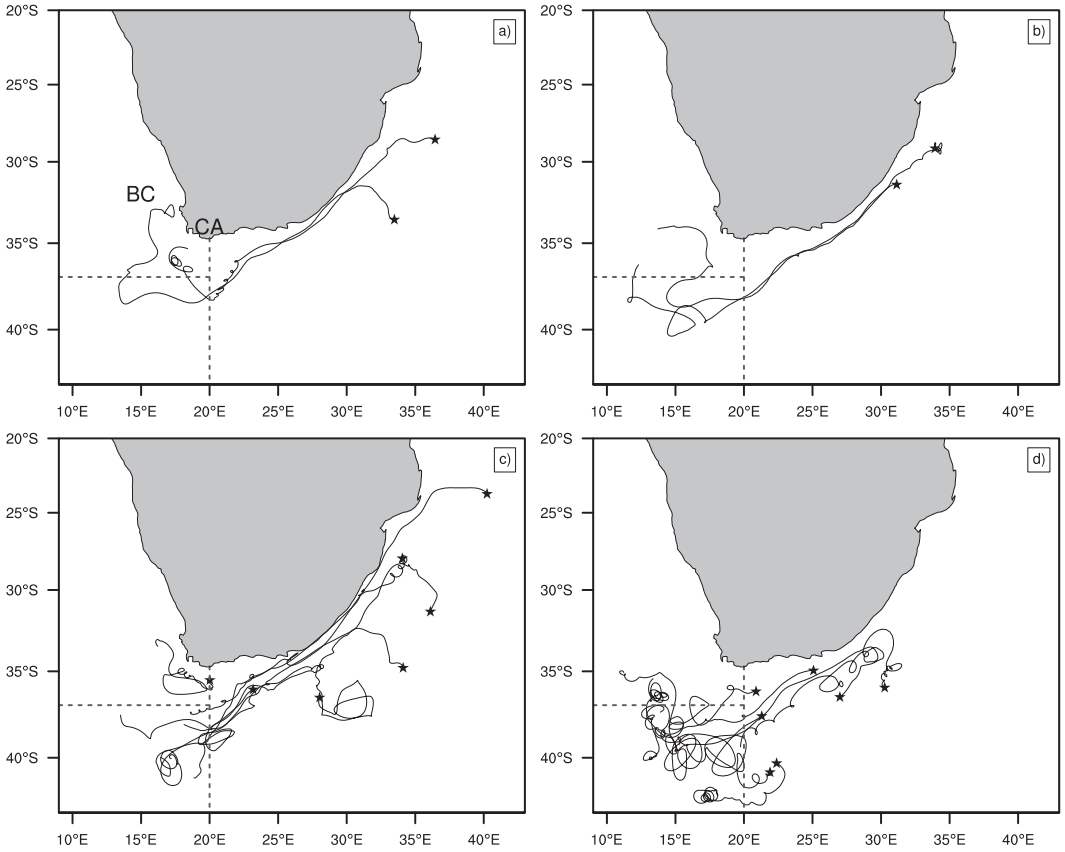

FIG. 9. Westward drifter crossings of the CA 20°E meridional (dashed) have been selected and separated in Rupolo Class (a) I (black), (b) II (green), (c) III (blue), and (d) IV (red). The start positions of the 64-day-long trajectories are indicated by black stars. Agulhas leakage is estimated from those drifters that cross the 37°S zonal (dashed) and continue northward with the Benguela Current (BC).

regimes, and, in particular, shows the composition of the dynamically complex Agulhas Current (mostly trajectories of a looping character, that is, Class III and IV).

The heat and salt transport from the Indian to the Atlantic Ocean (through surface eddies) influences the ocean circulation in the Atlantic Ocean and ultimately the circulation on a global scale (e.g., Beal et al. 2011). This process is also known as Agulhas leakage (cf., e.g., deRuiter et al. 2004; Richardson 2007), and the extent of the leakage has been estimated in percentages in relation to the total amount of trajectories crossing the Cape Agulhas (CA) meridional (fulfilled by 19 drifter segments) and the number of drifters continuing north of 37°S into the Atlantic Ocean (7 drifters, ~37%). These results are in agreement with those due to Richardson (2007) who estimated the Agulhas leakage from surface drifters (applying the same crossing criterions) to be around 33%.

The following subsections serve to show some concrete examples of how this trajectory data analysis method can be applied to study different dynamical systems; the Gulf Stream detachment area, the Kuroshio, and a subregion of the tropical Atlantic. A thorough analysis of these areas is beyond the scope of the present study. However, some results from the case studies will be offered. The regions were selected based on the previously presented results where the observed and modeled data differed substantially, and also because of their strategic locations in a global ocean circulation context.

1) THE GULF STREAM

In the first case, trajectory segments having starting positions west and south of the crossing point of the 35°N latitudinal and 75°W longitudinal [near Cape Hatteras (CH)] and end positions east and north of this limit were selected for analysis of the Gulf Stream detachment area (cf. Fig. 10). The slow ORCA1–5d currents (constituted mostly by Class-I trajectories) in Fig. 10b indicate an average surface-layer transport rather than the variable surface dynamics. The results

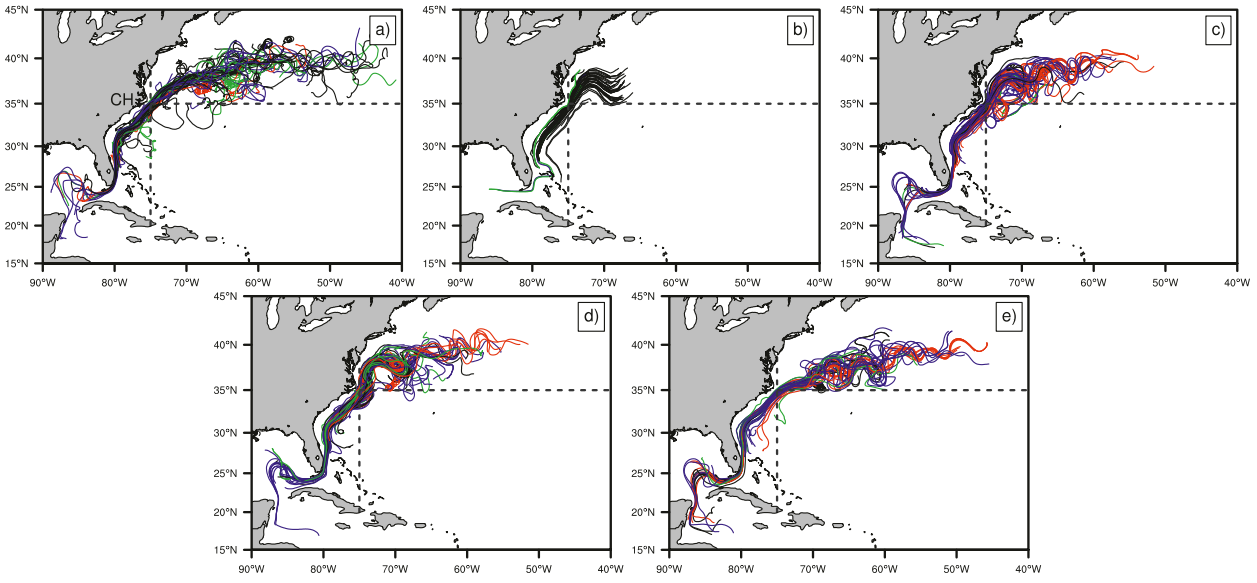

FIG. 10. (a) Observed, as well as synthetic (b) ORCA1–5d, (c) ORCA025–5d, (d) ORCA025–6h, and (e) ORCA12–5d northeastward trajectory crossings of the CH 35°N latitudinal and 75°W meridional. Rupolo classes are color coded as follows: Class I (black), II (green), III (blue), and IV (red).

from the ORCA025 configurations show great improvements of the modeled meandering and spreading of the Gulf Stream compared to the ORCA1–5d data (cf. Figs. 10c,d), and the best simulation of the current—in particular of the detachment angle off Cape Hatteras—is provided by the ORCA12–5d configuration (cf. Fig. 10e). Moreover, the coarser-grid model configurations tend to simulate a continued coastally bound current north of 35°N, in contrast to ORCA12–5d, that simulate accurately the northeasterly flow of the current directed across the North Atlantic Ocean.

The relative distributions of Rupolo classes for each dataset are presented in Fig. 13a (described in greater detail below), and from these results it is evident that the resolution of the horizontal grid is crucial in order to model the dynamics of the Gulf Stream properly. In fact, several previous studies indicate that an eddy-resolving horizontal grid resolution ($^1/_{10}°$ or higher) is necessary to obtain a realistic detachment of the Gulf Steam (cf., e.g., Chassignet and Marshall 2008). For an extensive study of observed and synthetic drifter-trajectory Lagrangian time scales in the North Atlantic compare, for example, Garraffo et al. (2001), Lumpkin et al. (2002), and Veneziani et al. (2004).

2) THE KUROSHIO

The second case deals with the Kuroshio off the east coast of Japan; a variable system where the path and EKE of the Kuroshio Extension modulate on decadal time because of oscillations between two dynamical states in the atmosphere over the North Pacific Ocean (cf. Qui and Chen 2010). Observed and modeled trajectories crossing the 34°N latitudinal and 144°E longitudinal from southwest to northeast were extracted from all datasets, and the results are presented in Fig. 11. The ORCA1–5d trajectories show large similarities with the results presented from the Gulf Stream area, with slowly progressing currents (Fig. 11b), while the realism of the velocity fields from the $^1/_4°$-resolution model is increased significantly in terms of absolute dispersion and structure of the current compared to ORCA1–5d (cf. Figs. 11c,d). The best representation of the dynamical regimes was obtained by the eddy-permitting and eddy-resolving configurations, as found from the relative Rupolo-class distributions in Fig. 13b (described in greater detail below). Furthermore, the ORCA12–5d data were the most realistic simulation of the Kuroshio detachment—near 35°N, 140°E—as well as the best representation of the current in terms of absolute dispersion (Fig. 11e).

3) THE TROPICAL ATLANTIC

The last case regards the equatorial surface currents in the tropical Atlantic, and trajectory segments with starting points within the Gulf of Guinea (±10°N and ±10°E), and end points west of the 10°W meridional were chosen for closer analyses. The observational data were found to be spread nearly symmetrically in two patches around the equator (Fig. 12a), namely in the Northern and Southern Equatorial Currents (cf., e.g., Lumpkin and Garzoli 2005). The observations from these two currents show distinct differences in dynamical

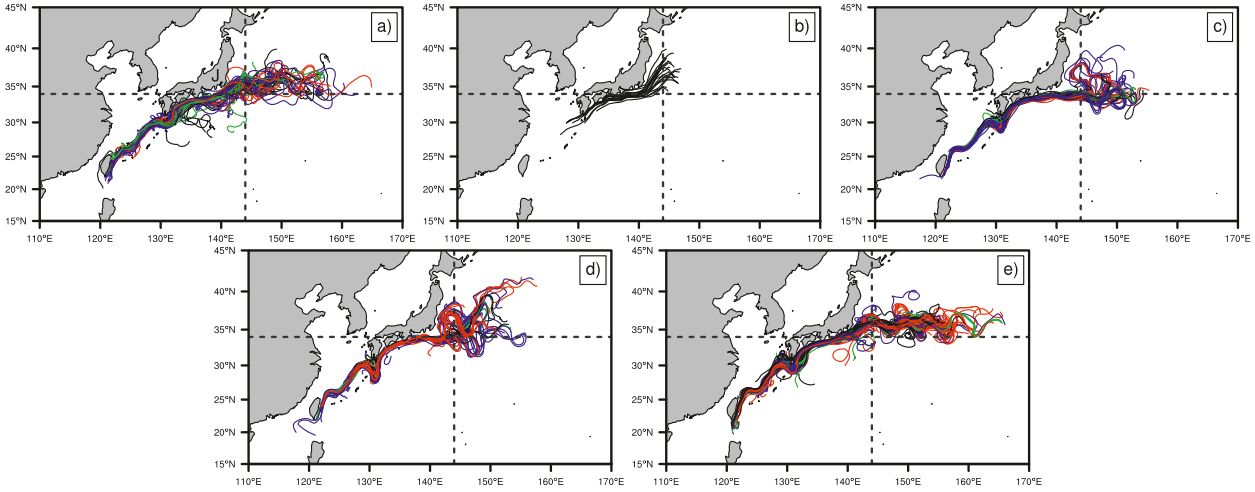

FIG. 11. (a) Observed, as well as synthetic (b) ORCA1–5d, (c) ORCA025–5d, (d) ORCA025–6h, and (e) ORCA12–5d northeastward trajectory crossings of the 34°N latitudinal and 144°E meridional in the Kuroshio detachment area off the Japanese (J) coast. Rupolo classes are color coded as follows: Class I (black), II (green), III (blue), and IV (red).

regimes, where meandering Class-III trajectories prevail in the northern and low-frequency motion Class-I trajectories in the southern patch. The general flow structures of the trajectories from the 5-day-average model fields were found to be relatively similar, and no clear improvement was discerned as the horizontal resolution of the models increased (cf. Figs. 12b,c,e). Furthermore, the 5-day-average model datasets were not capable of yielding the distinct difference between the synthetic northern and southern currents dynamical regimes. However, some sign of Rupolo-class separation was noted in the ORCA1–5d data (cf. Fig. 13c). In fact, according to the binned-average γ_R values in this region (cf. Fig. 4), the ORCA1–5d configuration provides the most accurate description of the dynamical regimes compared to drifter data and the other 5-day-average fields, with $\gamma_R \sim 1$ just north of the equator and lower values south.

The most realistic trajectory representation was obtained from the ORCA025–6h data that proved capable of capturing the different dynamical regimes north and south of the equator (cf. Fig. 12d) These findings imply that studies of ocean surface currents in this particular region are more sensitive to the time resolution of the dataset, rather than the size of the horizontal grid (the Class-I trajectories on the Southern Hemisphere being related to high-frequency perturbations, and thus more dependent on the averaging window of the model fields for a correct representation). This example illustrates, through the dynamical fingerprinting of ocean currents,

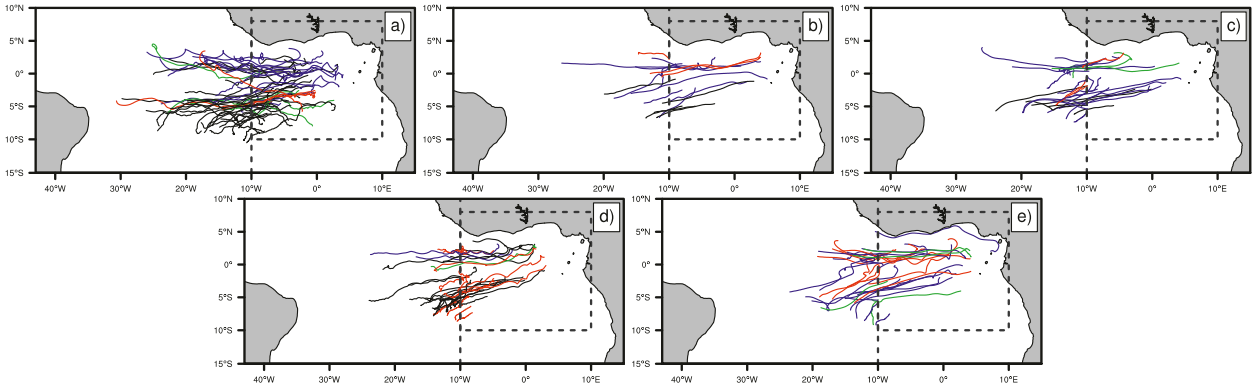

FIG. 12. (a) Observed, as well as synthetic (b) ORCA1–5d, (c) ORCA025–5d, (d) ORCA025–6h, and (e) ORCA12–5d trajectories starting in the Gulf of Guinea (dashed box) in the tropical Atlantic and crossing westward the 10°W meridional. Rupolo classes are color coded as follows: Class I (black), II (green), III (blue), and IV (red).

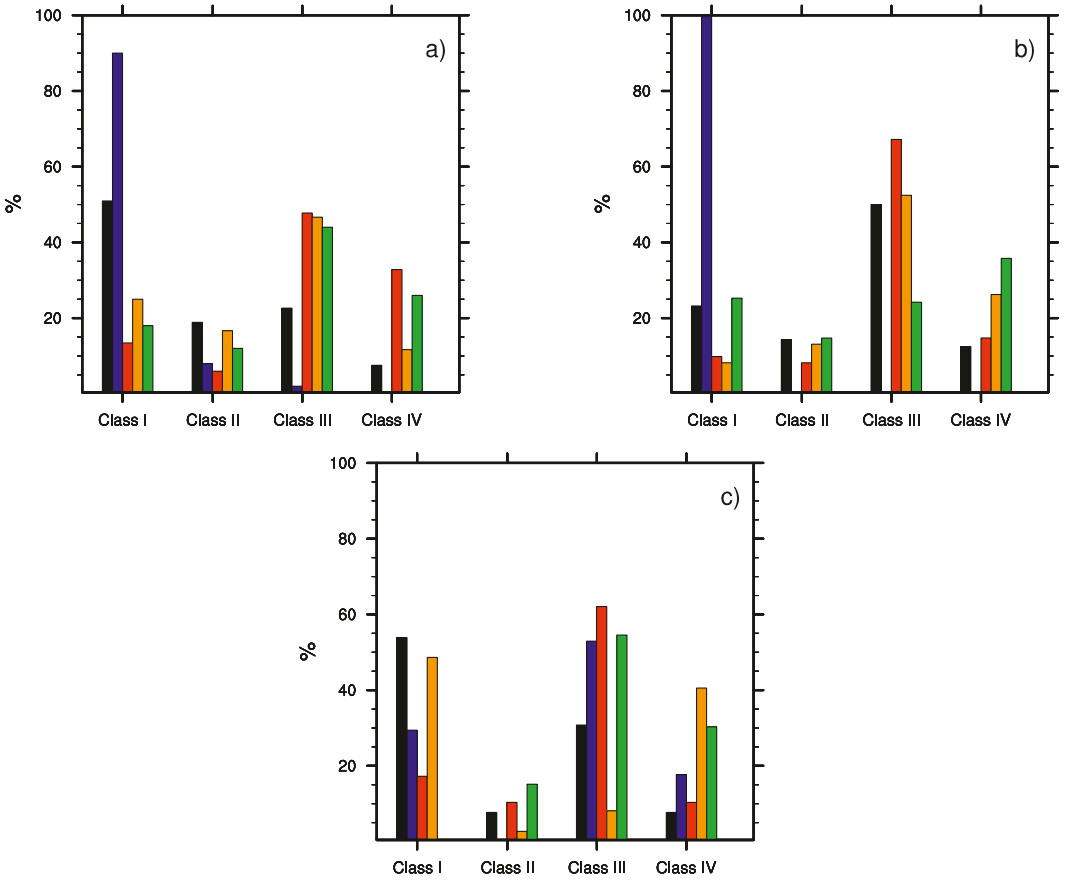

FIG. 13. Relative Rupolo-class distributions of the observed and modeled trajectories in the regional study regions: (a) Gulf Stream, (b) Kuroshio, and (c) the tropical Atlantic. The datasets are color coded as follows: Drifters (black), ORCA1–5d (blue), ORCA025–5d (red), ORCA025–6h (orange), and ORCA12–5d (green).

the relation between the westward equatorial currents in the northern Gulf of Guinea and the genesis of the Gulf Stream in the Caribbean Sea.

6. Summary and conclusions

When applying numerical methods for studies of ocean circulation, it is crucial to make the best trade off when it comes to choosing the size of the grid of the model configuration as well as the time-averaging window of the model output in relation to the characteristics of the dynamical features that are to be analyzed. In this study, surface velocity fields from three NEMO/ORCA grid configurations (noneddy-permitting ORCA1, eddy-permitting ORCA025, and eddy-resolving ORCA12) have been assessed, and the influence of the output frequency on the surface dynamics in ORCA025 has been evaluated. The analyses were undertaken in a Lagrangian framework where observed drifter tracks were confronted with model trajectories sharing the same start positions, and the Lagrangian time scales were estimated through stochastic modeling. The dispersal properties of the observations were found to be in full agreement with those presented by Rupolo (2007a), and his method for rationalizing ocean trajectory data proved to be very useful for evaluating the quality of the simulated surface dynamics by comparisons with drifter data. The results from the trajectory screening method and the subsequent scale separation of the data using the Rupolo ratio, were presented both as global-average distributions and as global turbulence maps for all model configurations. These maps can be used to identify areas where the time scales of the modeled ocean flow have been accurately resolved compared to observations.

Obviously, the coarse-grid ORCA1–5d model cannot resolve mesoscale characteristics of the ocean circulation (and consequently the modeled current systems tend to describe large-scale ocean transports). However, evaluating the modeled trajectory velocity time series in a Lagrangian framework could offer some additional insights on the simulated dynamics. While the absolute dispersion and the spectral analyses yielded rather poor

results, it was found that the global-average dynamical regimes were distributed in a reasonable manner compared to drifters (although local studies showed that this consonance was merely coincidental, with a few exceptions).

The global-average absolute dispersion improved when the model resolution was upgraded to the ORCA025 grid, and some further improvements were obtained applying the 6-h-average data compared to the 5-day model fields. Furthermore, it was found that the model output rate notably influences the velocity power spectral slope for the simulated trajectories, and the ORCA025 results gave (yet lacking generally in energy content) a more realistic slope at intermediate times when model fields were available every 6 h. Moreover, the results from the eddy-permitting ORCA025 configurations yielded reasonable global-average distributions of the simulated dynamical regimes, whereas the ORCA12–5d data showed an anomalously large amount of smooth looping trajectory data.

In conclusion, according to traditional Lagrangian analyses, the best representation of the global ocean dispersion and global-average spectral energy content would be provided by the eddy-resolving ORCA12–5d configuration, while the local characteristics of the surface turbulent flows were simulated in a more realistic manner by the ORCA025 configurations. The ORCA12–5d data, though accurately simulating the dynamical regimes of the western boundary currents and areas typically characterized by intense mesoscale dynamics, were found to comprise too-smooth trajectories in the interior of the basins. To eliminate the doubts that the excess smoothness is due to the 5-day sampling of the ORCA12 dataset, further analyses would be necessary with higher model data output frequencies, but because such data are not available at present, this matter will have to be dealt in a future study.

The Rupolo-ratio maps showed that the mesoscale motions in the North Atlantic Ocean and Arctic Sea were poorly simulated in all numerical models, and the reason for this could possibly be found within the unresolved acceleration time scales in this dynamically complex area, which is characterized by deep-convection and ice-formation processes. Another source of errors could be related to the 2D approximation of the synthetic Lagrangian trajectories, which could be less appropriate for detailed studies in convective areas. Local trajectory studies showed that the Gulf Stream and Kuroshio systems are reasonably well simulated by the ORCA025 and ORCA12 models, both in terms of dispersal properties and the turbulence regime distributions. The zoom in on the Gulf of Guinea in the tropical Atlantic indicated that this region, and, in particular, the Southern Equatorial Current, is more sensitive to the model output frequency compared to the other regions, possibly due to the variability of the atmospheric forcing along the equator.

EKE derived from binned-average drifter velocities can be considered a coarse first approximation of the eddy activity because it is not taking into account more than one turbulent regime in each subregion. However, EKE is often used as proxy for model parameterizations of eddy diffusivity (cf., e.g., Treguier et al. 2012). In this context, the trajectory separation analysis (based on a second-order LSM model) described in the present study could serve as an original complement as it provides detailed information of the underlying dynamics of the ocean currents and the turbulent composition of the flow. Mixing of different dynamical regimes can yield misleading results in terms of diffusion. Thus, it would be beneficial to evaluate the presence of one or more Rupolo classes in a certain subregion (and time frame, if seasonal differences are to be considered) before the velocity field can, to a first approximation, be considered homogeneous and a reliable estimate of diffusivity from the (re)distribution of eddy energy can be obtained.

Acknowledgments. Thanks are due to the two unknown reviewers for their constructive feedback on a previous version of the manuscript. J.A.U.N gratefully acknowledges the ENEA international fellowship program, which offered the possibility of undertaking the present study, and the International Meteorological Institute at Stockholm University for travel support during this period.

APPENDIX A

Stochastic Modeling

Dispersion studies in the ocean are usually considered in terms of Markovian LSM hierarchy (cf., e.g., Griffa 1996). The present study applies a second-order LSM model that is highly useful for studying Lagrangian motion in complex dynamical systems when the space and time scales of a phenomena are on the same order as the covered geographical area sampled by the drifter and the frequency of the observations; because it takes into account the finite space and time size of the effect of the random variables on the Lagrangian dispersion. The random discontinuity in second-order LSM models (also known as Markov-2 models) is introduced through the acceleration a, and the incremental equations are described by

$$\frac{dx}{dt} = U + u, \tag{A1}$$

$$\frac{du}{dt} = a - \frac{u}{T_v}, \quad \text{and} \tag{A2}$$

$$\frac{da}{dt} = -\frac{a}{T_a} + \kappa \frac{dw}{dt}, \tag{A3}$$

where $\kappa = \sqrt{2\sigma_U^2(T_a + T_v)}/T_v T_a$, σ_U^2 is the velocity variance, and T_v and T_a represent the characteristic velocity and acceleration time scales, respectively. Equations (A2) and (A3) are equivalent to the second-order stochastic process (cf. Sawford 1991):

$$\frac{d^2u}{dt^2} + \alpha_1 \frac{du}{dt} + \alpha_2 u = \kappa \frac{dw}{dt}, \tag{A4}$$

where $\alpha_1 = [(1/T_a) + (1/T_v)]$, $\alpha_2 = 1/T_a T_v$, and this model serve to correct the small-scale behavior of the first-order LSM in the description of flows at high, but finite, Reynolds numbers (Rupolo 2007b).

Integration of Eqs. (A1)–(A3) yield the velocity correlation function

$$R(t) = \frac{\beta_2 e^{\beta_1 |t|} - \beta_1 e^{\beta_2 |t|}}{\beta_2 - \beta_1} \quad \text{and} \tag{A5}$$

$$\beta_{1,2} = \frac{-\alpha_1 \pm \sqrt{\alpha_1^2 - 4\alpha_2}}{2}, \tag{A6}$$

where $\beta_{1,2}$ solves $z^2 + \alpha_1 z + \alpha_2 = 0$ and, in particular, $\beta_1 = -1/T_v$ and $\beta_2 = -1/T_a$ [following Sawford (1991)]. Furthermore, it can be shown (Berloff and McWilliams 2002) that $1/T_a T_v = \sigma_A^2/\sigma_U^2$, where σ_A^2 describe the acceleration variance, and that the Lagrangian correlation time T_L [Eq. (4)] is equal to $T_L = T_v[1 + (T_a/T_v)]$. The latter equality implies that when the acceleration time scale is nonzero, the finite acceleration contributes to increase the correlation of the velocity field (cf. Rupolo 2007a). Moreover, depending on the sign of the radicand in Eq. (A6), two different cases emerge: real T_a and T_v time scales when $\alpha_1^2 - 4\alpha_2 \geq 0$, and complex conjugate time scales when $\alpha_1^2 - 4\alpha_2 < 0$ (indicative of a missing important spatial dimension of the dynamics).

For $t \sim 0$, $R(t)$ is characterized by a smooth behavior, as is expected in flow with finite acceleration, while for $t \gg T_a$ the correlation function asymptotes to the exponential form characteristics of the first-order LSM. When $T_a > 0$ the variance of both velocity and acceleration is finite, while when $T_a \to 0$ Eq. (A3) becomes a first-order equation and the model collapses to a first-order LSM. The velocity power spectrum [Eq. (2)] is typically characterized by a plateau for low frequencies, decreasing with a variable logarithmic slope in the intermediate-frequency range (cf. Fig. 3); for a detailed discussion on these matters see Rupolo (2007b).

APPENDIX B

The Lagrangian Trajectory Code TRACMASS

TRACMASS is a well-established open-source code for analytical offline computations of advected Lagrangian trajectories from two- or three-dimensional velocity fields from both atmospheric and oceanic GCMs (Döös 1995; Blanke and Raynaud 1997; Blanke et al. 2001). The trajectory code was first developed within the European project TRACMASS, and after its conclusion in 2001, the code has been subject to continuous elaborations and improvements (de Vries and Döös 2001; Döös and Engqvist 2007).

In particular, for model velocities on a C grid, volume transports are calculated across the grid cells by integrating linearly over the opposite walls. The volume transport across the eastern wall of an *ijk* grid cell is described by $F_{ijk} = u_{i,j,k}\Delta y \Delta z_k$ (the meridional transports are obtained similarly), and i, j, and k refer to the discretized longitude, latitude, and depth, respectively. In our study, we have applied a 2D approximation of the velocity field in order to obtain 15-m-depth model trajectories comparable with the drifter observations. Thus, the k-level and Δz_k values in TRACMASS were kept constant. The zonal direction of the trajectories is provided by the following discretization

$$F(r) = F_{i-1,j,k} + (r - r_{i-1})(F_{i,j,k} - F_{i-1,j,k}), \tag{B1}$$

where the particle positions $r = x/\Delta x$, the local transports are related as $F = dr/ds$, and s is defined as time scaled by the *ijk* grid cell volume $\Delta x \Delta y \Delta z_k$. These relations can be written as a homogenous linear differential equation and by applying an initial condition, here $r(s_0) = r_0$, the equation can be solved analytically. Thus, the zonal displacement inside a grid cell is described by

$$r(s) = \left(r_0 + \frac{\beta}{\alpha}\right) e^{-\alpha(s - s_0)} - \frac{\beta}{\alpha}, \tag{B2}$$

where $\alpha \equiv F_{i-1,j,k} - F_{i,j,k}$ and $\beta \equiv -F_{i-1,j,k} - \alpha r_{i-1}$. Finally, the time when a trajectory reaches a zonal wall is obtained explicitly by

$$s_1 = s_0 - \frac{1}{\alpha}\log\left(\frac{r_1 + \frac{\beta}{\alpha}}{r_0 + \frac{\beta}{\alpha}}\right), \tag{B3}$$

and $r_1 = r(s_1)$ is given by either of the particle positions, r_{i-1} or r_i. The meridional (and vertical, in those cases 3D trajectories are being considered) displacements of the trajectories inside the grid cells are calculated analogously, and by considering the smallest transit time Δs and its corresponding particle position r_1, the trajectory exit wall is yielded along with the point of entry in the neighboring cell.

Thus, these Lagrangian trajectories correspond to the passive advection of a zero-dimension particle by the velocity fields from the ocean circulation model, and no subgrid parameterizations or additional diffusion have been added such as, for example, random walk. The integration is performed on an hourly basis for the 5-day- and 6-h-average model fields, thus providing model trajectory points at the same rate as the observed drifter positions.

Dispersal properties of TRACMASS-integrated trajectories were compared with those of surface drifters for the World Ocean by Döös et al. (2011) and for the Baltic Sea by Kjellsson and Döös (2012). Moreover, recent updates involve applications in marine-ecological (Corell et al. 2012) and risk-assessment studies of nearshore radionuclide spreading in the proximity of planned nuclear-waste repositories (Corell and Döös 2013). The software is available online for the scientific community (http://tracmass.org/), and has been applied by, for example, van Sebille et al. (2009, 2011), in their studies of mesoscale dynamics in the dispersive Agulhas region.

REFERENCES

Babiano, A., and A. Provenzale, 2007: Coherent vortices and tracer cascades in two-dimensional turbulence. *J. Fluid Mech.,* **574,** 429–448, doi:10.1017/S0022112006004265.

Barnier, B., and Coauthors, 2006: Impact of partial steps and momentum advection schemes in a global ocean circulation model at eddy-permitting resolution. *Ocean Dyn.,* **56,** 543–567.

Beal, L., and Coauthors, 2011: On the role of the Agulhas system in ocean circulation and climate. *Nature,* **472,** 429–436, doi:10.1038/nature09983.

Berloff, P., and J. C. McWilliams, 2002: Material transport in oceanic gyres. Part II: Hierarchy of stochastic models. *J. Phys. Oceanogr.,* **32,** 797–830.

Blanke, B., and S. Raynaud, 1997: Kinematics of the Pacific Equatorial Undercurrent: An Eulerian and Lagrangian approach from GCM results. *J. Phys. Oceanogr.,* **27,** 1038–1053.

——, S. Speich, G. Madec, and K. Döös, 2001: A global diagnostic of interocean mass transfers. *J. Phys. Oceanogr.,* **31,** 1623–1632.

Brodeau, L., B. Barnier, A.-M. Treguier, T. Penduff, and S. Gulev, 2010: An ERA-40-based atmospheric forcing for global ocean circulation models. *Ocean Modell.,* **31,** 88–104, doi:10.1016/j.ocemod.2009.10.005.

Chassignet, E., and D. Marshall, 2008: *Gulf Stream Separation in Numerical Ocean Models. Geophys. Monogr.,* Vol. 177, Amer. Geophys. Union, 39–61.

Corell, H., and K. Döös, 2013: Difference in particle-transport patterns between an open and a closed coastal area in the Baltic Sea: High-resolution modeling with advective particle trajectories. *Ambio,* **42,** 455–463.

——, P.-O. Moksnes, A. Engqvist, K. Döös, and P. Jonsson, 2012: Larval depth distribution critically affects dispersal and the efficiency of marine protected areas. *Mar. Ecol. Prog. Ser.,* **467,** 29–46, doi:10.3354/meps09963.

Davies, R. E., 1991: Lagrangian ocean studies. *Annu. Rev. Fluid Mech.,* **23,** 43–64.

deRuiter, W. P. M., H. M. van Aken, E. J. Beier, J. R. E. Lutjeharms, R. P. Matano, and M. W. Schouten, 2004: Eddies and dipoles around South Madagascar: Formation, pathways and large-scale impact. *Deep-Sea Res. I,* **51,** 383–400.

de Vries, P., and K. Döös, 2001: Calculating Lagrangian trajectories using time-dependent velocity fields. *J. Atmos. Oceanic Technol.,* **18,** 1092–1101.

Döös, K., 1995: Interocean exchange of water masses. *J. Geophys. Res.,* **100** (C7), 13 499–13 514.

——, and A. Engqvist, 2007: Assessment of water exchange between a discharge region and the open sea—A comparison of different methodological concepts. *Estuarine Coastal Shelf Sci.,* **74,** 585–597.

——, V. Rupolo, and L. Brodeau, 2011: Dispersion of surface drifters and model-simulated trajectories. *Ocean Modell.,* **39,** 301–310, doi:10.1016/j.ocemod.2011.05.005.

Elhmaidi, D., A. Provenzale, and A. Babiano, 1993: Elementary topology of two-dimensional turbulence. *J. Fluid Mech.,* **242,** 655–700.

Elipot, S., and S. T. Gille, 2009: Estimates of wind energy input to the Ekman layer in the Southern Ocean from surface drifter data. *J. Geophys. Res.,* **114,** C06003, doi:10.1029/2008JC005170.

Garraffo, Z. D., A. J. Mariano, A. Griffa, C. Veneziani, and E. P. Chassignet, 2001: Lagrangian data in a high-resolution numerical simulation of the North Atlantic I. Comparison with in situ drifter data. *J. Mar. Syst.,* **29,** 157–176.

Gent, P. R., and J. C. Mcwilliams, 1990: Isopycnal mixing in ocean circulation models. *J. Phys. Oceanogr.,* **20,** 150–155.

Griffa, A., 1996: Applications of stochastic particle models to oceanographic problems. *Stochastic Modelling in Physical Oceanography,* R. Adler, P. Müller, and B. Rozovskii, Eds., Birkhäuser., 113–140.

——, K. Owens, L. Piterbarg, and B. Rozovskij, 1995: Estimates of turbulence parameters from Lagrangian data using a stochastic particle model. *J. Mar. Syst.,* **53,** 371–401.

Grodsky, S. A., R. Lumpkin, and J. A. Carton, 2011: Spurious trends in global surface drifter currents. *Geophys. Res. Lett.,* **38,** L10606, doi:10.1029/2011GL047393.

Hansen, D. V., and P.-M. Poulain, 1996: Quality control and interpolations of WOCE-TOGA drifter data. *J. Atmos. Oceanic Technol.,* **13,** 900–909.

Hua, B. L., J. McWilliams, and P. Klein, 1998: Lagrangian accelerations in geostrophic turbulence. *J. Fluid Mech.,* **366,** 151–176.

Jackson, L., R. Hallberg, and S. Legg, 2008: A parameterization of shear-driven turbulence for ocean climate models. *J. Phys. Oceanogr.,* **38,** 1033–1053.

Killworth, P. D., 2008: Estimating bolus velocities from data—How large must they be? *J. Phys. Oceanogr.,* **39,** 70–88.

Kjellsson, J., and K. Döös, 2012: Surface drifters and model trajectories in the Baltic Sea. *Boreal Environ. Res.,* **17,** 447–459.

LaCasce, J., 2008: Statistics from Lagrangian observations. *Prog. Oceanogr.,* **77,** 1–29.

Lumpkin, R., and S. L. Garzoli, 2005: Near-surface circulation in the Tropical Atlantic Ocean. *Deep-Sea Res. I,* **52,** 495–518.

——, and M. Pazos, 2007: Measuring surface currents with Surface Velocity Program drifters: The instrument, its data, and some recent results. *Lagrangian Analysis and Prediction of Coastal and Ocean Dynamics (LAPCOD),* A. Griffa et al., Eds., Cambridge University Press, 39–67.

——, A. Treguier, and K. Speer, 2002: Lagrangian eddy scales in the northern Atlantic Ocean. *J. Phys. Oceanogr.,* **32,** 2425–2440.

Madec, G., and Coauthors, 2012: NEMO ocean engine, version 3.4. Institut Pierre-Simon Laplace Note du Pole de Modelisation 27, 357 pp.

Mariano, A., and E. H. Ryan, 2007: Lagrangian analysis and prediction of coastal and ocean dynamics (LAPCOD). *Lagrangian Analysis and Prediction of Coastal and Ocean Dynamics (LAPCOD),* A. Griffa et al., Eds., Cambridge University Press, 423–479.

McClean, J. L., P.-M. Poulain, J. W. Pelton, and M. E. Maltrud, 2002: Eulerian and Lagrangian statistics from surface drifters and a high-resolution POP simulation in the North Atlantic. *J. Phys. Oceanogr.,* **32,** 2472–2491.

Niiler, P. P., and J. D. Paduan, 1995: Wind-driven motions in the Northeast Pacific as measured by Lagrangian drifters. *J. Phys. Oceanogr.,* **25,** 2819–2830.

Pasquero, C., A. Provenzale, and A. Babiano, 2001: Parameterization of dispersion in two-dimensional turbulence. *J. Fluid Mech.,* **439,** 279–303.

Qui, B., and S. Chen, 2010: Eddy-mean flow interaction in the decadally modulating Kuroshio Extension system. *Deep-Sea Res. II,* **57,** 1098–1110.

Richardson, P. L., 2007: Agulhas leakage into the Atlantic estimated with subsurface floats and surface drifters. *Deep-Sea Res. I,* **54,** 1361–1389.

Rio, M.-H., 2012: Use of altimeter and wind data to detect the anomalous loss of SVP-type drifter's drogue. *J. Atmos. Oceanic Technol.,* **29,** 1663–1674.

Rupolo, V., 2007a: A Lagrangian-based approach for determining trajectories taxonomy and turbulence regimes. *J. Phys. Oceanogr.,* **37,** 1584–1609.

——, 2007b: Observing turbulence regimes and Lagrangian dispersal properties in the ocean. *Lagrangian Analysis and Prediction of Coastal and Ocean Dynamics (LAPCOD),* A. Griffa et al., Eds., Cambridge University Press, 231–274.

——, B. L. Hua, A. Provenzale, and V. Artale, 1996: Lagrangian spectra at 700 m in the western North Atlantic. *J. Phys. Oceanogr.,* **26,** 1591–1607.

Sawford, B. L., 1991: Reynolds number effects in Lagrangian stochastic models of turbulent dispersion. *Phys. Fluids A,* **3,** 1577–1586.

Taylor, G., 1921: Diffusion by continuous movements. *Proc. London Math. Soc.,* **20,** 196–212.

Treguier, A. M., I. M. Held, and V. D. Larichev, 2012: Parameterization of quasigeostrophic eddies in primitive equation ocean models. *J. Phys. Oceanogr.,* **27,** 567–580.

van Sebille, E., C. N. Barron, A. Biastoch, P. J. van Leeuwen, F. C. Vossepoel, and W. P. M. de Ruijter, 2009: Relating Agulhas leakage to the Agulhas Current retroflection location. *Ocean Sci.,* **5,** 511–521.

——, L. Beal, and W. E. Johns, 2011: Advective time scales of Agulhas leakage to the North Atlantic in surface drifter observations and the 3D OFES model. *J. Phys. Oceanogr.,* **41,** 1026–1034.

Veneziani, M., A. Griffa, A. Reynolds, and A. Mariano, 2004: Oceanic turbulence and stochastic models from subsurface Lagrangian data for the northwest Atlantic Ocean. *J. Phys. Oceanogr.,* **34,** 1884–1906.